ELSEVIER

Challenges and improvement pathways to develop quasi-1D $(Sb_{1-x}Bi_x)_2Se_3$-based materials for optically tuneable photovoltaic applications. Towards chalcogenide narrow-bandgap devices

Ivan Caño [a,*], Pedro Vidal-Fuentes [b], Axel Gon Medaille [b], Zacharie Jehl [a], Alex Jiménez-Arguijo [b], Maxim Guc [b], Victor Izquierdo-Roca [b], Claudia Malerba [c], Matteo Valentini [c], Maykel Jiménez-Guerra [a], Marcel Placidi [a], Joaquim Puigdollers [a], Edgardo Saucedo [a]

[a] Escola d'Enginyeria de Barcelona Est (EEBE), Universitat Politècnica de Catalunya, Av. Eduard Maristany, 16, 08019, Barcelona, Spain
[b] Institut de Recerca en Energia de Catalunya (IREC), Jardins de les Dones de Negre, 1, 08930, Sant Adrià del Besòs, Spain
[c] Italian National Agency for New Technologies, Energy and Sustainable Economic Development (ENEA), Lungotevere Thaon di Revel, 76, 00196, Roma, Italy

ARTICLE INFO

ABSTRACT

Quasi-1D chalcogenides have shown great promises in the development of emerging photovoltaic technologies. However, most quasi-1D semiconductors other than Sb_2Se_3 and Sb_2S_3 have been seldom investigated for energy generation applications. Indeed, cationic or anionic alloying strategies allow changing the bandgap of these materials, opening the door to the development of an extended range of chalcogenides with tuneable optical and electrical properties. In this work, Bi incorporation into the Sb_2Se_3 structure has been proved as an effective approach to modulate the bandgap between <1.0 eV and 1.3 eV, demonstrating conversion efficiencies between 3 and 5% for $0.01 < x \leq 0.10$. However, there is a noticeable deterioration in optoelectronic parameters for $x > 0.1$. In order to better understand the underlying mechanisms leading to the formation of $(Sb_{1-x}Bi_x)_2Se_3$, and thus design specific strategies to enhance its properties, thin films with different annealing time and temperature have been synthesized and characterized. Interestingly, it has been observed that Sb_2Se_3 and Bi_2Se_3 are formed first, with Bi melting at 300 °C and diffusing rapidly towards the surface of the film. At higher temperature, the binary compounds combine to form the solid solution, however as the dwell time increases, $(Sb_{1-x}Bi_x)_2Se_3$ decomposes again into Bi_2Se_3 and Sb. This study has shown that the material is essentially limited by compositional disorder and recombination via defects. Likewise, routes have been proposed to improve morphology and uniformity of the layer, achieving efficiencies higher than 1% for $x > 0.2$.

1. Introduction

An escalating interest in the integrative implementation of PV devices into building elements (requiring transparency, such as windows or glass-based façades), as well as into flexible and lightweight applications (such as for textiles, flexible IoT devices or roof tiles), has raised awareness of the need to develop disruptive materials and technologies suitable for high-efficiency and optically tuneable (transparent, semi-transparent) solar harvesters [1]. These novel technologies could open new market opportunities, broadening the fields of PV applications, along with allowing their integration into multi-junction configurations, moving forward towards targeting efficiency values beyond the single junction Shockley-Queisser limit at about 33% [2].

In the light of all this, quasi-1D chalcogenides have shown great potential to become a breakthrough, offering an innovative and revolutionary approach to boost up the photovoltaic performance of thin-film-based devices, owing to their unique capacity to exhibit enhanced anisotropic electrical properties in extremely thin materials when they are correctly oriented, as well as their unusually large absorption co-efficients [3]. The structure of quasi-1D materials consists of covalently bonded ribbons along one crystallographic direction, while stacked together by weak van der Waals interactions in the other two directions, hence conferring strong anisotropic optoelectronic properties along the covalently-bonded ribbons (such as preferential carrier transport). Thus,

by tuning the crystalline orientation of quasi-1D thin films it is possible to increase their minority carrier mobility and collection, therefore improving the photovoltaic (PV) performance of the device [4]. Among these semiconductors, Sb_2Se_3 has shown great promise, achieving an auspicious 9.2% power conversion efficiency (PCE) in substrate configuration. Also, it is constituted by simple earth-abundant components, leading to nontoxic and stable solar cells. Sb_2S_3 and $Sb_2(S,Se)_3$ have also been studied to some extent, achieving efficiencies beyond 7% and 10.5% respectively [5–7]. However, despite the very attractive properties and steady improvements in PCE, the performance of Sb_2Se_3-based devices is limited by a high V_{oc} deficit, suggesting that recombination processes involving deep defects may be a limiting factor [8–10].

Furthermore, 1D semiconductors beyond Sb_2Se_3 have been barely investigated for energy generation applications, hence the limits to their potential have not yet been reached. In fact, a number of quasi-1D semiconductors for solar harvesting applications can be available. As a rule, in order to ensure the crucial covalent bonding leading to ribbon-like structure, the difference between electronegativities of cations and anions needs to be lower than 1.7 eV. Based on that, several chalcogenides, halides and mixed chalcogenide/halide compounds can be devised comprising a broad bandgap range and the potential to develop attractive optoelectronic properties for PV, including $Sb_2(S,Se)_4$, (Sb,Bi) SI or BiSBr [11,12]. However, most of these materials have relatively wide bandgaps above 1.5 eV, see Fig. 1, which could be certainly useful for specific applications (such as manufacturing tandem solar cells with Si or semi-transparent devices) [13–15]. Notwithstanding, it is also interesting to investigate narrow-bandgap materials. Indeed, ideal tandem efficiencies can be achieved by combinations of $E_{g1} = 0.9$ eV and $E_{g2} > 1.5$ eV [16]. Also, narrow bandgaps are highly interesting for architectures combining three or more cells. Therefore, obtaining quasi-1D semiconductors with bandgap in the range 0.9–1.1 eV could further expand their potential applications, moving forward the development of innovative materials with tuneable optical and electrical properties.

Fig. 1 shows the bandgaps of different chalcogenide and mixed chalcogenide/halide technologies, including the successful Sb_2Se_3 system (see Table 1). Note that most mixed halides and sulphides have bandgaps above 1.5 eV (up to 3 eV). Hence, they have the potential to develop relatively wide bandgap devices. On the other hand, Bi_2Se_3 possesses a very narrow bandgap of 0.3–0.6 eV, which makes it

Table 1

Summary of the bandgaps of chalcogenide/halides semiconductors (literature values).

Compound	Bandgap (eV)	References
BiOBr	2.7–3.0	[17,18]
SbSI	2.2–2.4	[19–22]
SbSBr	2.0–2.2	[19,23]
BiSBr	1.95–2.0	[18,19,24]
BiOI	1.75–1.8	[17]
SbSeI	1.7–1.75	[23,25]
Sb_2S_3	1.7–1.75	[6,19]
$Sb_2(S,Se)_3$	1.1–1.75	[7,19,26]
Bi_2S_3	1.3–1.7	[19,27,28]
$Sb_{0.67}Bi_{0.33}SI$	1.6–1.65	[29]
BiSI	1.55–1.6	[19,25,30,31]
BiSeBr	1.5–1.55	[18,24]
BiSeI	1.25–1.3	[18,25,32]
Sb_2Se_3	1.1–1.3	[5,33–35]
$(Sb,Bi)_2Se_3$	0.9–1.2	[36–38]
Bi_2Se_3	0.3–0.6	[39,40]

especially suitable for thermoelectricity [41]. However, Bi_2Se_3 is stable in a treadymite (rhombohedral Bravais lattice, and $R3m$ space group) two-dimensional structure, whereas the alternative orthorhombic phase is metastable and difficult to obtain [39,42,43]. In fact, vacuum-based techniques have mostly led to pure rhombohedral Bi_2Se_3 [44,45], while electrodeposition methods result in a mixture of rhombohedral and orthorhombic phases [43,46,47]. Significantly, it has been reported that Sb-alloying causes an spontaneous structural transition from rhombohedral to orthorhombic. Accordingly, a pure rhombohedral $(Sb_{1-x}Bi_x)_2Se_3$ phase appears for large Bi amounts (x > 0.8), which has aroused interest as a topological insulator [48,49]. Instead, when x < 0.6, the material holds a single-phase orthorhombic structure similar to Sb_2Se_3. Finally, for 0.6< x < 0.8, coexistence of both structures is detected [36–38,50,51]. Interestingly, in the x < 0.6 range, a decrease in the bandgap is observed upon Bi incorporation, reaching values as low as 0.9 eV, see Fig. 1 (red bar), placing the $(Sb_{1-x}Bi_x)_2Se_3$ alloy as an optimum quasi-1D alternative to develop high efficiency tandem devices assembled with any $E_g > 1.5$ eV absorber [16].

Despite its clear potential as a narrow-bandgap photoabsorber, $(Sb_{1-x}Bi_x)_2Se_3$ has been barely studied for photovoltaics. So far, a device with 0.93 eV bandgap and x = 0.43 was reported to yield 132.5 mV V_{oc} and 18.4 mAcm^{-2} J_{sc}, resulting in a 0.7% power conversion efficiency (PCE); the low V_{oc} attributed to either a back contact barrier blocking the extraction of photocurrent or due to poor carrier transport within the bulk [36]. However, a comprehensive study on the evolution of optoelectronic properties upon increasing Bi incorporation could shed further light on the challenges to develop $(Sb_{1-x}Bi_x)_2Se_3$-based solar cells, the effect of Bi on the material growth and properties, as well as point towards the optimum composition to achieve devices with 0.9–1.0 bandgap and good PV performance.

In this study, a scalable sequential procedure based on the selenization of thermally evaporated Bi/Sb stack has been designed to synthesize $Mo/(Sb_{1-x}Bi_x)_2Se_3$ thin films with an extended compositional span, from x = 0.01 to x = 0.3 – within the range which allows to tune the bandgap between 0.9 and 1.2 eV. These samples have been thoroughly characterized by current density-voltage (JV) measurements (illuminated and dark), internal quantum efficiency (IQE), X-ray diffraction (XRD) and Raman spectroscopy. Accordingly, the material has been shown to undergo a steep decline in the optoelectronic properties when x > 0.1, which is likely due to greater recombination via defects within the bulk upon Bi incorporation. In particular, the two-diode model has been used to study in detail the optoelectronic parameters, demonstrating that there is a correlation between higher disorder, compositional inhomogeneity, and an increasing ideality factor (free from all constraints from the model). Additionally, Raman spectroscopy and XRD have shown that Bi is effectively incorporated into the
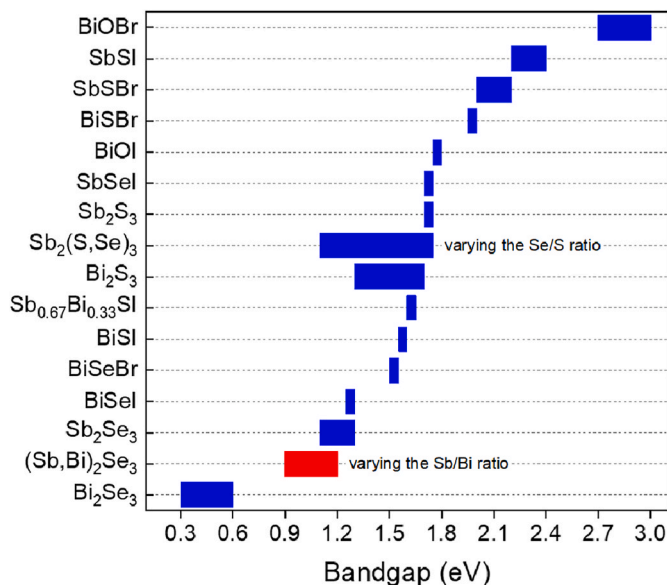

Fig. 1. Bandgap (eV) of chalcogenides and mixed chalcogenide/halide semiconductors.

solid solution, but there is a compositional gradient in depth due to Bi distribution, which tends to diffuse towards the surface of the layer.

In order to understand the underlying mechanisms that lead to the formation of the $(Sb_{1-x}Bi_x)_2Se_3$ solid solution, and thus design specific strategies to enhance the properties of the material and improve its PV performance, thin films with different annealing times and temperature have been synthesized, offering an overview of the phases that are formed in each synthesis step, their crystalline quality and their morphology. As a result, it has been observed that the binary compounds Sb_2Se_3 and Bi_2Se_3 are formed first, with Bi_2Se_3 appearing at lower temperatures. As temperature increases, the formation of the solid solution takes place, with Bi fully incorporated into the Sb_2Se_3 orthorhombic structure. Finally, if the annealing dwell time and/or temperature continue increasing, the $(Sb_{1-x}Bi_x)_2Se_3$ compound will decompose, resulting in Se sublimation and the appearance of Bi_2Se_3 and α-Sb_2O_3 phases.

Hence, here we present clear evidence on how the $(Sb_{1-x}Bi_x)_2Se_3$ forms, and how it decomposes over time. With this knowledge, optimal synthesis conditions have been proposed, and changes have been implemented to improve the material's morphology, with which we have achieved for the first time (to the best of our knowledge), an $(Sb_{1-x}Bi_x)_2Se_3$ photovoltaic devices with PCE between 3 and 5% for $0.01 < x \leq 0.10$, and greater than 1% for $x \geq 0.2$. These results, and the extensive study of materials properties, point the way to further improve $(Sb_{1-x}Bi_x)_2Se_3$-based thin films for narrow-band photovoltaic, showing that the potential of quasi-1D chalcogenides is still far from being reached.

2. Experimental procedure

2.1. Materials and devices preparation

$(Sb_{1-x}Bi_x)_2Se_3$ polycrystalline thin films were manufactured on Mo sputtered SLG substrates (SLG/Mo), using a scalable sequential process consisting in the following steps. First, Bi was deposited by thermal evaporation (Oerlikon Univex 250), using Bi powder (Aldrich, 100 mesh 99%), a base vacuum of 10^{-5} mbar and evaporation rate of 0.3 Å/s. Then, Sb was also deposited by thermal evaporation onto the Mo/Bi metal stack from Sb shots (Alfa Aesar, 1–3 mm diameter), with a base vacuum of 10^{-5} mbar and evaporation rate of 1 Å/s [52,53]. The multilayer Mo/Bi/Sb system thus constitutes the metallic precursor for the synthesis of $(Sb_{1-x}Bi_x)_2Se_3$. The nominal composition of the layer is established by deposition of different Bi and Sb thicknesses, so that variable x indicates the overall Bi content. For example, for the $(Sb_{0.8}Bi_{0.2})_2Se_3$ sample, the density of the sample was determined as 0.4 $\rho_{Bi_2Se_3} + 1.6$ $\rho_{Sb_2Se_3}$, with which the necessary molar amount of each element was calculated for a total thickness of 800 nm; the stoichiometry of the film was used to compute the content by weight of Bi and Sb, and their densities allowed to determine that the evaporated thickness should be 80 nm and 272 nm respectively. The same procedure was followed for the samples with different composition, considering the appropriate x for each case. See Table S1 for the thicknesses of the metallic stack in all cases. Next, the SLG/Mo/Bi/Sb precursors were cut into pieces of 2×1.5 cm^2 and subjected to Se reactive annealing in a tubular furnace, using a glass Petri dish (15 cm^3 volume) containing 8 mg Se powder (Alfa Aesar, 99.9995%), homogeneously distributed around the sample in the centre of the dish. Additionally, the tube was filled with argon to provide an inert atmosphere and to control the system pressure. Samples were heated up to 340 °C with a 20 °C/min heating ramp at 500 mbar, annealed during 30min at this temperature, and then cooled down naturally (60 min approximately). For the formation mechanism study, the thermal process conditions were modified according to the criteria discussed further in the main text.

Photovoltaic devices are fabricated with the device stack adapted from Sb_2Se_3 solar cells [52], which is SLG/Mo/$(Sb_{1-x}Bi_x)_2Se_3$/CdS/i-ZnO/ITO. n-type CdS buffer was deposited by chemical bath deposition,

followed by i-ZnO + ITO deposition by DC-pulsed magnetron sputtering (Alliance Concept CT100). Individual solar cells were defined by mechanical scribing (Micro Diamond MR200 OEG), with a scribe line width of 20 nm.

2.2. Materials and devices characterization

Nominal composition and thickness of the as-synthesized $(Sb_{1-x}Bi_x)_2Se_3$ absorbers were determined by X-ray fluorescence spectroscopy (XRF) with a Fischerscope XVD equipment, which was previously calibrated by ICP-MS. Phase content characterization by Raman spectroscopy was performed with an optical probe developed at IREC, coupled to a FHR640 Horiba Jobin Yvon spectrometer, where the signal was collected by a liquid nitrogen cooled CCD detector. The measurements were performed in back scattering configuration using HeNe gas laser (632.8 nm) as excitation source, focused on a macro spot (~50 μm), and with optical penetration depth of 50 nm (being the absorption coefficient of Sb_2Se_3 films around 10^5 cm^{-1}) [53]. Laser power density was kept under 25mWcm^{-2} to avoid degradation of the films. The X-ray diffraction (XRD) patterns were acquired with a Bruker D8 Advance equipment in Bragg–Brentano configuration, using CuKα radiation and 2θ range from 10° to 80°, with step size of 0.02°. Diffractograms were analysed with X'Pert HighScore software. SEM micrographs were obtained in cross-section configuration (by mechanical cleavage of the full device) using a Zeiss Series Auriga field-emission microscope, with an acceleration voltage of 5 kV and working distances ranging between 3 and 5 mm.

In-depth chemical composition profiles of the thin films were investigated by Glow Discharge Optical Emission Spectroscopy (GDOES), using a Horiba Jobin Yvon GD Profiler 2 spectrometer equipped with an anode diameter of 4 mm, 19 channels for fixed elements and an additional channel for an arbitrary element; and cross-sectional analysis by energy dispersive X-ray spectroscopy (EDX), using an INCAPentaFETx3 detector. Micrographs have been prepared by focused ion beam (FIB), by means of a CANION31 Ga FIB column.

Current-voltage characteristics (JV curves) were characterized under dark and illumination conditions using simulated AM1.5G spectrum from a Sun 3000 AAA-class Abet solar simulator, showing uniform illumination area of 15×15 cm^2 (previously calibrated with Si reference cell). Dark JV curves were fitted according to the two-diode model of a solar cell. Quantum efficiency measurements were performed using a Bentham PVE300 system calibrated with Si and Ge photodiodes. Internal quantum efficiency (IQE) curves were derived from external quantum efficiency (EQE) and optical reflectivity measurements (in accordance with Equation S1), which were performed with integrated sphere and transmittance UV–Vis spectroscopy equipment.

Finally, the modelling of $(Sb_{1-x}Bi_x)_2Se_3$ solar cells was performed using SCAPS 3.308 software and a set of material parameters from various literature sources, considering a 1000 nm thick absorber with a material stack similar to that of experimental devices, with the aim to obtain a qualitative verification of the hypotheses made from laboratory data [54]. The nature of the defects was specifically modelled after the work reported by *Chen* et al. [55], while the bulk defect concentration was varied within a range of 10^{13}cm^{-3} to 10^{18}cm^{-3}. As the model does not claim to be a quantitative representation of the experimental devices, optical properties and bandgap variations are ignored, which allows to limit the number of interplaying parameters and streamlines the conclusions regarding the shape of the IQE curves.

3. Study of $(Sb_{1-x}Bi_x)_2Se_3$ thin films optoelectronic and structural properties as a function of the Bi amount (x)

3.1. Optoelectronic characterization and simulations

A complete study has been carried out on the optoelectronic properties of $(Sb_{1-x}Bi_x)_2Se_3$ as a function of the Bi amount (ranging from x =

0 to x = 0.30). Accordingly, Mo/$(Sb_{1-x}Bi_x)_2Se_3$/CdS/i-ZnO/ITO devices were prepared following the previously described experimental procedure. Results from this study are shown in Fig. 2a–d, where the PCE, J_{sc}, V_{oc} and fill factor (FF) have been plotted as a function of Bi content (x). It is observed that between x = 0 and x = 0.1 the J_{sc} increases sequentially, while the V_{oc} decreases, which is consistent with the expected decline in the bandgap by incorporating Bi to the Sb_2Se_3 structure [56,57]. Also, PCE between 3 and 5% have been demonstrated for 0.01 < x ≤ 0.10. Nevertheless, for x > 0.1, there is a noticeable deterioration of the optoelectronic parameters, with J_{sc} and V_{oc} decreasing abruptly, and PCE declining to values slightly above 0 (0.3%). In order to further investigate the performance of $(Sb_{1-x}Bi_x)_2Se_3$ devices, IQE measurements were performed, see Fig. 2e and f. In Fig. 2e, it is observed that devices with x = 0 and x = 0.01 present similar IQE curves, indicating that a very low Bi amount has been effectively incorporated into Sb_2Se_3, without significantly modifying the bandgap or the electronic structure of the material. Increasing x to 0.05 and 0.1, the IQE intensity decreases slightly and extends to higher λ values, denoting a smaller bandgap. Also, the fact that the IQE maximum appears at 700 nm suggests that there is recombination at the interface, causing the efficiency to decrease for the high photon energy range, as discussed in more detail below [58]. Finally, for x = 0.2 and x = 0.3, the overall IQE decreases dramatically, in line with the aforementioned PCE sharp decline. Interestingly, when applying a negative bias voltage, the IQE intensity escalates to higher values, see Fig. 2f, and with −0.5V bias, they virtually recover the performance of pure Sb_2Se_3. This demonstrates that the deterioration in the PCE of $(Sb_{1-x}Bi_x)_2Se_3$ solar cells is not caused by a loss of the intrinsic PV effect. Instead, a possible explanation is that the device becomes progressively limited by a diminishing carrier diffusion length. The fact that the IQE intensity increases drastically when a negative bias voltage is applied supports this hypothesis, since increasing the space charge region may allow photogenerated carriers to reach their respective transport layers despite the smaller diffusion length [59]. Therefore, it is possible that $(Sb_{1-x}Bi_x)_2Se_3$ with x > 0.1 are essentially limited by bulk recombination, leading to shorter carrier lifetime and diffusion length, hence dramatically reducing the PV performance of devices.

From the IQE, the electronic bandgap was obtained as a function of the Bi amount (x), see Fig. 2g. As expected, the bandgap decreases sequentially as x increases, confirming that it can be modulated between 1.0 and 1.23 eV by incorporating Bi into the Sb_2Se_3 structure, and thus

proving the potential of $(Sb_{1-x}Bi_x)_2Se_3$ to develop chalcogenide-based narrow bandgap devices. Also, the decreasing trend is not linear, but rather follows a polynomial curve ($Eg = 1.23 – 1.03x + 1.16x^2$), which concurs with previous results reported by *P. Weiss* et al. [36].

Additionally, a deeper analysis of $(Sb_{1-x}Bi_x)_2Se_3$ optoelectronic properties was performed by fitting dark JV curves using the two-diode model (Fig. S1). Accordingly, series resistance (R_s), ideality factors and dark saturation currents (n_1 and $I_{0,1}$ for diode 1, n_2 and $I_{0,2}$ for diode 2 respectively) were estimated, see Fig. 3. Dark JV curves fitting was performed using two methodologies. First, the ideality factors were assumed to be $n_1 = 1$ and $n_2 = 2$ (fixed values), hence the experimental dark JV curves were fitted under these restrictions, albeit releasing all other parameters (thus far only considering recombination via single recombination centres) [60]. As a result, the series resistance and saturation currents were determined. Regarding the series resistance, note that it remains at relatively small values when the Bi amount stays below x < 0.01 (1.8 Ωcm^2 and 1.9 Ωcm^2 for x = 0 and x = 0.01 respectively), but increases linearly with a 17 Ωcm^2 slope as a larger Bi content is incorporated, reaching $R_s = 5.1$ Ωcm^2 for x = 0.2, see Fig. 3a. The larger series resistance might result from nonoptimal contact alignment or to a poor carrier transport within the bulk of the absorber, which in turn could result from reduced electron and hole mobility due to an increased concentration of bulk defects [36,61]. Similarly, from the calculated saturation currents it has been confirmed that Bi incorporation leads to increased bulk recombination. Indeed, it is observed that the saturation current $I_{0,2}$ is significantly higher than $I_{0,1}$ (3–4 orders of magnitude), and increases continuously, presenting a linear trend between x = 0.1 and x = 0.3, see Fig. 3b. The two-diode model allows to account for the contribution of Shockley-Read-Hall (SRH) recombination mechanisms via defects into the bandgap, by means of which the recombination rate slope and subsequently also the recombination current slope have a factor of 2 (ideality factor n = 2), see Equation S2 [60,62]. In turn, the saturation current I_0 can be interpreted as a recombination parameter, since when multiplied by an excitation factor (the normalized *pn* product), it allows to determine the cumulative recombination expressed as a current [63]. Therefore, the fact that $I_{0,2}$ is larger than $I_{0,1}$ (where $n_2 = 2$) suggests that the principal recombination mechanism limiting the performance of the device is SRH-based (defect assisted), demonstrating that higher Bi amounts lead to greater recombination via defects within the absorber's space charge region (n_2 ideality factor originates from a situation where n ≈ p, thus it

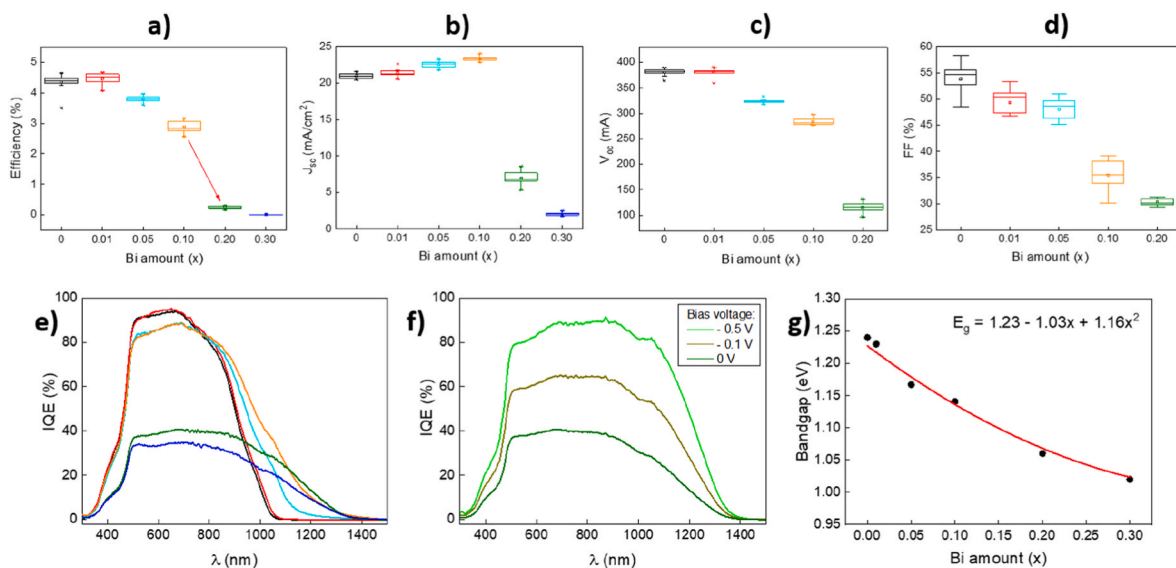**Fig. 2.** Optoelectronic parameters of Mo/$(Sb_{1-x}Bi_x)_2Se_3$/CdS/i-ZnO/ITO solar cells as a function of Bi amount (x): **a)** PCE, **b)** J_{sc}, and **c)** V_{oc} **d)** FF. **e)** IQE curves of Mo/$(Sb_{1-x}Bi_x)_2Se_3$/CdS/i-ZnO/ITO solar cells as a function of Bi amount (x). **f)** IQE curves of Mo/$(Sb_{0.8}Bi_{0.2})_2Se_3$/CdS/i-ZnO/ITO solar cells with applied bias voltage (0 V, −0.1 V, −0.5 V). **g)** Bandgap as a function of Bi amount (x).
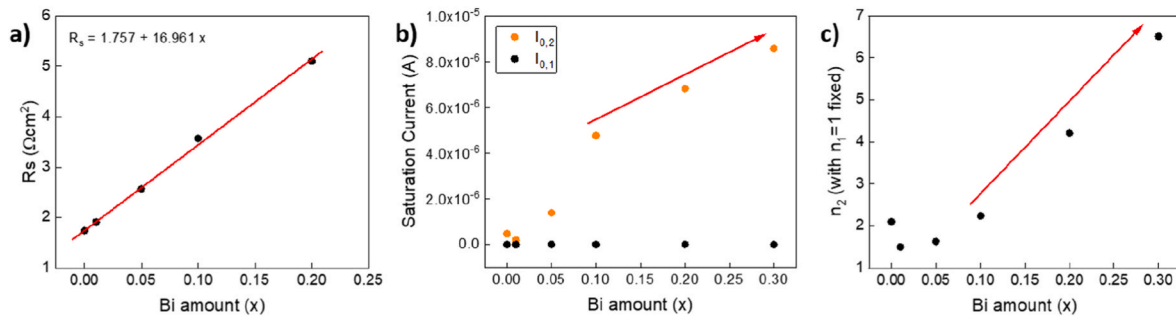
Fig. 3. a) Series resistance of Mo/(Sb$_{1-x}$Bi$_x$)$_2$Se$_3$/CdS/i-ZnO/ITO solar cells as a function of Bi amount (x). b) Saturation currents I$_{0,1}$ and I$_{0,2}$ Bi amount (x). c) Ideality factor n$_2$ as a function of Bi amount (x), computed assuming that n$_1$ = 1. Values obtained using a two-diode model software.

accounts mostly for the effect of recombination in the depletion zone) [60]. The nature of these defects will be discussed further.

Secondly, dark JV curves were fitted reducing the model restrictions to n$_1$ = 1, thus freeing n$_2$ from any constraint. With this, it is possible to evaluate the degree of adjustment with the two-diode model, and the contribution of phenomena resulting in n$_{id}$>2. For instance, it is noted that the JV curves of (Sb$_{1-x}$Bi$_x$)$_2$Se$_3$ films with x = 0 to x = 0.1 can be fitted successfully with n$_2$ = 1.5 to 2, indicating good agreement with the two-diode model and prevalence of recombination processes via single recombination centres. Nonetheless, for x = 0.2 and x = 0.3, n$_2$ increases to 4.2 and 6.5 respectively, see Fig. 3c. Such large ideality factors can occur as a result of multistep recombination channels via a series of trap states distributed along the bandgap. These non-ideal recombination current contributions are due to an increased number of defects, such as edge currents or non-linear shunts anywhere in the cell. If the density of these defects is sufficiently high, carriers can recombine through more than one defect, leading to multistep recombination and currents with n > 2 [64–66]. In the case of (Sb$_{1-x}$Bi$_x$)$_2$Se$_3$, it has been shown that the higher Bi content leads to increased defect concentration, which in turn possibly results in increased multistep recombination processes. Also, a higher n$_2$ factor might provide an indication of disorder originating from a heterogeneous distribution of cations (Bi and Sb), causing the appearance of band tails, and hence deteriorating the overall device performance. The suggested effect of substitutional disorder is furtherly discussed in the structural characterization section.

The previous hypotheses have been evaluated by SCAPS software simulations, modelling a baseline (Sb$_{0.8}$Bi$_{0.2}$)$_2$Se$_3$ device by using state of the art parameters and a defect profile inspired by *Y. Chen* et al. [67] and *A. Gon Medaille* et al. [68], where the bulk defect density is the only floating parameter. The primary goal of this study is to examine how the shape and intensity of IQE curves are changed as a function of the concentration of defects at the interface and bulk of the absorber. It is not a quantitative analysis. Instead, we focus on the critical parameter (i. e., defect density), and demonstrate that this parameter yields the

changes that are observed experimentally. For that purpose, bandgap variations, band alignment and other features of the device are assumed irrelevant and thus ignored in the model, establishing a baseline such that these factors do not interfere with the conclusions of the study.

Fig. 4a and b displays a situation where the bulk defect density is increased from a value of 5·10^{13} cm^{-3} up to 5·10^{18} cm^{-3}, Indeed, the evolution of the modelled IQE curves displays a behaviour similar to that observed in the experiments. When the bulk defect density is low enough to be irrelevant compared to the interface defects and those dominate, the IQE value is lower in the high photon energy range than it is in the low photon energy range. This particular shape tackles a common misconception in the field that interface defects are a loss mechanism affecting all carriers equally in the IQE analyses [69]. Such statement is demonstrably untrue from the fact that indeed, under monochromatic illumination, electron-hole (e-h) pairs are statistically generated at different absorber depths as a function of the incident wavelength. For high photon energy, the e-h pairs will be primarily generated in the space charge region, at the vicinity of the pn junction. These pairs are thus subjected to interface recombination, as both carrier types are present in a small absorber volume. Otherwise, for a lower photon energy, e-h carriers are generated deeper in the absorber, well beyond the space charge region. As the illumination is monochromatic and few holes are present in the space charge region, this imbalance leads to photoelectrons reaching the pn junction not recombining through interface defects and, therefore, the low energy part of the IQE (800 nm–1000nm) reaches higher values than the high energy part (500 nm–700nm) –, see Fig. S2 for the modelled photocarrier density as a function of position within the film, illustrating that carriers are generated deeper in the absorber when using a low energy excitation, while a high energy excitation leads to increased carrier generation at the vicinity of the pn junction (1 μm). In line with this principle, it is confirmed that (Sb$_{1-x}$Bi$_x$)$_2$Se$_3$ films with low Bi amounts (x = 0 to x = 0.1) are essentially limited by interface recombination, see Fig. 2d.

On the other hand, it should be noted that under a white light bias of enough intensity, which generates a continuous depth-distribution of
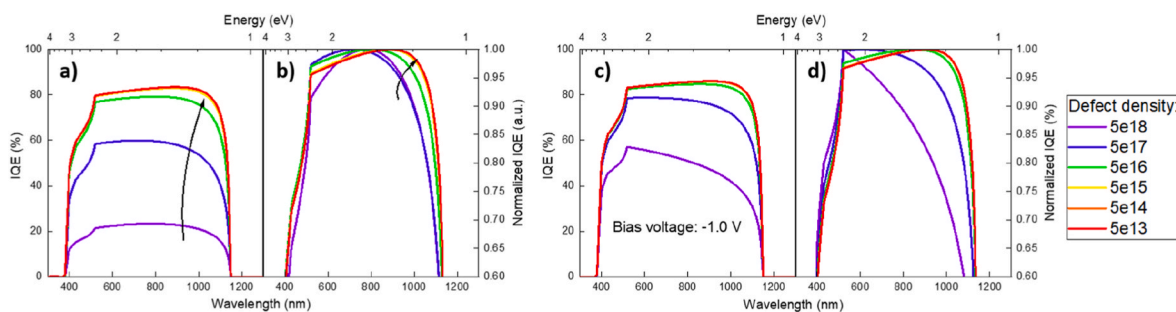

Fig. 4. **a)** Modelled IQE curves without applied bias for a (Sb,Bi)$_2$Se$_3$ solar cell with fixed interface defects and variable density of bulk defects. **b)** Normalized IQE curves. **c)** Modelled EQE curves with a −1.0 V external bias for a (Sb,Bi)$_2$Se$_3$ solar cell with fixed interface defects and variable density of bulk defects. **d)** Normalized IQE curves.

photocarriers in the absorber, the aforementioned statement that interface defects affect all carriers equally becomes true, but this is beyond the scope of the current discussion.

When increasing the bulk defect density, the minority carrier diffusion length in the absorber becomes reduced, therefore significantly affecting the overall IQE values and giving the curve a bell-like shape, clearly visible in the normalized curves, see Fig. 4b. The previous statement regarding interface defects and e-h pairs generated at the vicinity of the pn junction remains true, and interface defects are the predominant recombination pathway in the high photon energy range. Alternatively, in the low photon energy range (850 nm–1050nm), a decreasing number of photocarriers are able to reach the interface due to the smaller diffusion length, resulting in the characteristic decrease of the IQE curve. The maximum IQE value is thus obtained in the 750 nm–800nm range, where photoelectrons can still diffuse to the pn junction without being affected by interface defects in the absence of holes.

In Fig. 4c and d, a similar analysis is carried out with IQE curves calculated under a constant -1V external bias, which slightly expands the space charge region width while significantly increasing the electric field, and thus the selectivity of the contact. The conditions in which bulk defect density is high benefit the most from such configuration, with the IQE spectrum remarkably increasing and its shape being much more triangular, as photoelectrons able to reach the depletion region are more efficiently collected. Otherwise, the IQE curves calculated for conditions in which interface defects dominate and bulk defects are irrelevant are only marginally affected by the application of an external bias, as expected from the previous discussion. Significantly, these results show a clear correspondence with the experimental IQE spectra from Fig. 2e.

Note that while the ideas developed in this simple model do not unequivocally demonstrate our hypotheses regarding the increasing prevalence of bulk defects in the presence of Bi, they represent a strong argument in that direction, and are consistent with the previously discussed fitting results of experimental dark JV curves.

3.2. Structural characterization

Complementing the previous study, SLG/Mo/$(Sb_{1-x}Bi_x)_2Se_3$ samples (similar to the ones used for optoelectronic characterization before) were manufactured to perform structural characterization by Raman spectroscopy analysis and XRD, see Fig. 5. The average Raman spectra of bare $(Sb_{1-x}Bi_x)_2Se_3$ thin films ($0 < x < 0.3$) are shown in Fig. 5a, where the peaks with an asterisk correspond to the orthorhombic Sb_2Se_3 phase

[70–72], and the blue dotted lines indicate the rhombohedral Bi_2Se_3 phase (orthorhombic Bi_2Se_3 is metastable) [46,73]. The estimated optical penetration depth of the applied excitation wavelength is around 50 nm, which allows to conclude that interface and close to interface structural changes have the main impact on the analysed Raman spectra. The comparison of Raman spectra of samples with x = 0 and x = 0.01 shows no significant differences between them, with only a slight increase of the width of the peaks, most probably related with small distortions of the lattice due to partial substitution of Sb cations by Bi, which is, however, not enough to produce detectable changes in the spectrum related to the solid solution formation. The later starts to be well pronounced for the sample with x = 0.05, where a shoulder at the red side of the main Sb_2Se_3 peak has appeared. The appearance of this shoulder and its further red shift was previously correlated with the appearance of the $(Sb_{1-x}Bi_x)_2Se_3$ solid solution [37]. Taking into account the expected structural similarity of the Sb_2Se_3 and Bi_2Se_3 (metastable) orthorhombic phases, the observed shoulder can be tentatively assigned to the A_g-like mode, which is the second mode (peak at 192 cm^{-1} is the first one) in a two mode behaviour system of the $(Sb_{1-x}Bi_x)_2Se_3$ solid solution with orthorhombic structure [74]. Also, the position of the peak related to the discussed shoulder allows to estimate the Sb/Bi ratio [37], which was found to be close to the nominal compositions. Together with the shoulder evolution, new peaks have appeared in the samples with x $\geq$ 0.05 (72 and 138 cm^{-1}), which also exhibit a clear increase of intensity with increasing Bi content. These peaks can be assigned to the A_{1g} and E_g modes of pure rhombohedral Bi_2Se_3, which is likely present at the surface of all samples with x $\geq$ 0.05 [73]. Note that the third peak, usually observed in rhombohedral Bi_2Se_3 close to 175 cm^{-1}, is not so pronounced owing to a strong overlap with other peaks. Considering the presence of the pure Bi_2Se_3 phase, and that estimated Sb/Bi ratios were close to nominal values, it is logical to assume the presence of pure Sb_2Se_3. However, no other secondary phases, such as elemental Sb, Se, or SbO_3, have been detected.

In order to further characterize the structural properties of the $(Sb_{1-x}Bi_x)_2Se_3$ phase, XRD analysis was carried out on bare Mo/$(Sb_{1-x}Bi_x)_2Se_3$ samples, see Fig. 5b (complete diffractogram in Fig. S3). Diffraction peaks can be either indexed either to the orthorhombic Sb_2Se_3 (ICDD 04-003-0715) or the rhombohedral Bi_2Se_3 (ICDD 01-077-1715) structures, in addition to Mo from the back contact. Significantly, by incorporating Bi, no phase transition is observed. Indeed, all peaks correspond to the orthorhombic crystal structure and no rhombohedral Bi_2Se_3 peaks have been detected, indicating that for Bi amounts which x $\leq$ 0.3, the $(Sb_{1-x}Bi_x)_2Se_3$ solid solution retains the original orthorhombic structure of Sb_2Se_3 – the fact that the Raman analysis revealed the presence of Bi_2Se_3
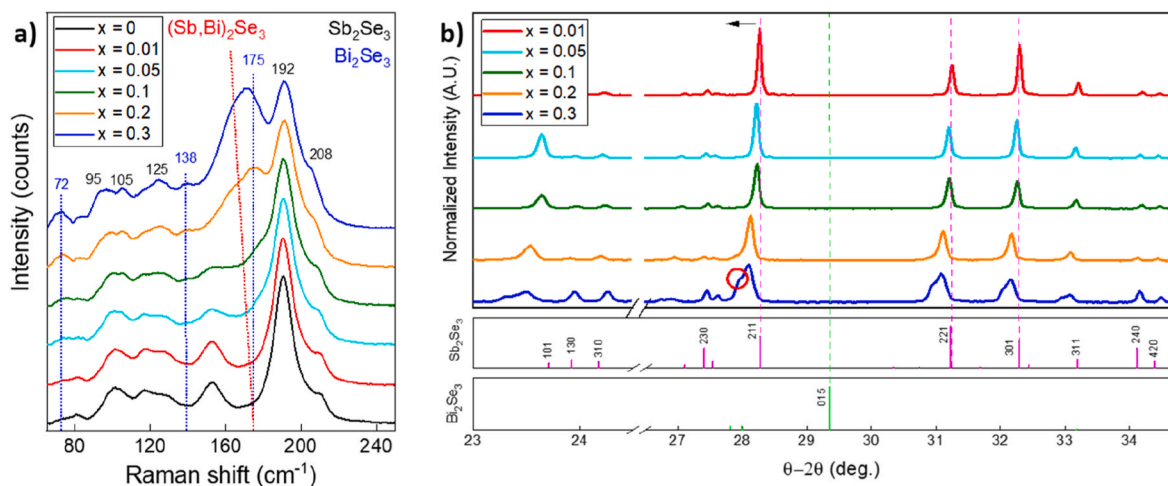

Fig. 5. a) Normalized Raman spectra of the surface of $(Sb_{1-x}Bi_x)_2Se_3$ thin films as a function of Bi amount (x). **b)** X-ray diffractograms of selected Mo/$(Sb_{1-x}Bi_x)_2Se_3$ samples as a function of Bi amount (x).

indicates that in a small amount this phase may be present on the surface. However, as the Bi content increases, the orthorhombic crystal lattice experiences deformations (which is expected due to the larger ionic radius of Bi occupying Sb positions), resulting in the following diffractogram variations:

- (hkl), (h0l), (0 kl) and (00l) peaks [with h,k,l≠0] shift towards smaller 2θ values. E.g., see the Bragg reflection at 28.2° in Fig. 5b, successively shifting towards lower 2θ as the Bi amount increases.
- (hk0) peaks shifts towards higher 2θ values (e.g., see peaks at 23.9° and 24.1° in Fig. 5b).

Moreover, as Bi incorporation increases, the $(Sb_{1-x}Bi_x)_2Se_3$ XRD peaks widen and a shoulder appears systematically to their left – which can be observed in all (hkl), (h0l), (0 kl) and (00l) reflections –, being especially noticeable in the samples with large Bi amounts (x = 0.3, x = 0.2). For example, the red circle in Fig. 5b indicates a shoulder, or peak overlapping feature, appearing to the left of the 28.2° Bragg reflection. The fact that this feature appears repeatedly throughout the whole diffractogram, and that it is not accompanied by any additional peaks, suggests that it is neither the result of a phase transition (which would lead to different crystalline structure), nor secondary phases. However, it might point to an inhomogeneous distribution of Bi, resulting in a solid solution gradient. By GDOES measurements it has been indeed shown that Bi content is higher near the surface, decreasing progressively towards the back contact, see Fig. S4. In addition, a FIB cross-section of the $(Sb_{0.8}Bi_{0.2})_2Se_3$ film was analysed by EDX linescan mapping, confirming the results of GDOES, i.e., shows a decreasing profile in the Bi amount from the sample, see Fig. S5. This observation leads to two principal conclusions. First, that the Bi initially deposited on Mo tends to diffuse towards the surface during the annealing process. Second, the existence of a compositional gradient in depth implicates variations to the lattice parameters of $(Sb_{1-x}Bi_x)_2Se_3$ (which depend on the amount of Bi replacing Sb), causing the widening and peak overlapping detected by XRD.

Finally, incorporation of Bi also causes a deterioration of the crystalline orientation. Owing to their van der Waals structure, quasi-1D semiconductors present anisotropic optoelectronic properties, resulting in increased carrier mobility along the c-axis (ribbon-assisted transport) [4]. Hence, favoured orientation in the [00l] direction (along the c-axis according to *Pbnm #62*) is desirable to develop enhanced carrier transport properties. Here, the texture coefficient (TC, see Equation S3) has been used to study the evolution of preferred orientation by increasing the Bi amount [75,76]. Texture coefficient along the [002] direction is higher in samples with lower Bi amount, while high Bi amount samples have lower TC_{002}, indicating loss of crystalline growth in the desired orientation (3.9 for x = 0.01, 1.4 for x = 0.3), see Table S2a. On the other hand, as x increases, so does TC_{230} (0.1 for x = 0.01, 0.7 for x = 0.3). Note that in the case of (230)-oriented materials, the sum of *h* and *k* Miller indices is larger than 3, suggesting lateral growth (angles between covalent ribbons and the substrate are small). It is shown that Bi incorporation (x < 0.3) leads to a deterioration of the optimum crystalline orientation for enhanced c-axis conductivity [75, 76].

3.3. Interpretation of results

So far, optoelectronic and structural analyses have shown that increasing the Bi amount leads to $(Sb_{1-x}Bi_x)_2Se_3$ films being increasingly limited by bulk recombination, increased disorder (due to inhomogeneous distribution of cations), and loss of the 00l-preferred crystalline orientation. Regarding the effect of bulk recombination, the results here presented are consistent with DFT calculations developed by *Cai Z.* and *Chen S.*, according to which Bi in Sb_2S_3 (due to chemical similarities, an akin behaviour is expected for Sb_2Se_3) occupies antisite positions (Bi_{Sb}) and interstices (Bi_i). The formation energy of Bi_{Sb} is extremely low,

indicating a high solubility of Bi; however, it is a neutral defect and thus not expected to affect the electrical properties of the absorber such as doping (still, the bandgap is expected to change). On the other hand, Bi_i have a higher formation energy, acting as donor defects and producing a deep carrier recombination centre in the bandgap [77]. Therefore, by incorporating a very small Bi amount into the $Sb_2(S,Se)_3$ system, we expect that mainly Bi_{Sb} antisites will appear due to their low formation energy, without significantly interfering with device performance. Nevertheless, by increasing the Bi content, Bi will begin to occupy Bi_i positions, resulting in increased defect-assisted recombination and reduced photoconductivity (Bi_i is donor and can act as a trap for electrons), which in turn will decrease the carrier diffusion length and cause an increase of saturation current and ideality factor, agreeing with the experimental results and optoelectronic characterization above. Indeed, we deem essential to continue studying the nature of Bi-related defects in chalcogenides, moving towards a larger understanding of their formation and impact, and thus design specific strategies to overcome their detrimental effect on devices.

Furthermore, structural characterization has shown that Bi tends to diffuse towards the surface during annealing, resulting in an inhomogeneous compositional distribution, which in turn involves a bandgap gradient (lower near the surface, higher in the back). Also, a decrease in the texture coefficient along the (00l) direction has been observed by increasing Bi content, which can negatively affect the mobility of carriers. In order to understand the underlying mechanisms that lead to the formation of the solid solution, and therefore devise methodologies to improve its properties and performance, a synthesis study has been carried out by means of interrupted growth, i.e., $(Sb_{0.8}Bi_{0.2})_2Se_3$ thin films have been prepared with different annealing time and temperatures, following a specific sequence destined to procure an overview of the phases that are formed in each stage of the synthesis process, their crystalline quality and their morphology, see Fig. 6.

4. Study of $(Sb_{0.8}Bi_{0.2})_2Se_3$ formation via interrupted growth

The interrupted growth experiment has been performed with a single composition of x = 0.2, which was selected because it belongs to the range showing a noticeable compositional gradient (see XRD results in Fig. 5), while exhibiting bandgap in the spectrum of interest (1.05 eV) for the development of narrow-bandgap devices. XRF analysis of the films revealed that for treatments with no dwell time, it is likely that the material is not completely selenized, resulting in thinner samples and x > 0.2, see Table S3. Otherwise, as temperature and dwell time increase, we obtain samples with ~700 nm thickness and stable composition around x = 0.20; apart from very long times (6 h), when the Bi amount x increases notably and thickness sinks to ~380 nm, indicating possible decomposition.

Raman analysis provides valuable information on the development of the phases during the material's synthesis process. For example, at stage 1 (Fig. 6, t1), only peaks of Sb_2Se_3 with preferentially horizontal ribbon alignment – [hk0] orientation – are detected [78]. The ribbons preferred orientation at low synthesis temperature is in accordance with previous Sb_2Se_3 results [79]. Absence of Bi or Bi_2Se_3 signals might be related with not sufficient temperature to react the subjacent Bi layer, or to allow Bi to diffuse towards the surface (heed that Raman spectroscopy is a surface sensitive technique). Therefore, only Sb selenization is occurring at 250 °C. At 300 °C (Fig. 5, t2), peaks of rhombohedral Bi_2Se_3 (strong signals at 72, 130 and 175 cm^{-1}) are seen in the Raman spectrum along with the peaks from the orthorhombic phases of pure Sb_2Se_3 and maybe of $(Sb_{1-x}Bi_x)_2Se_3$ solid solution with small amount of Bi. It is likely that at this temperature there is enough Se partial pressure to react throughout the thickness of metal precursor, but only part of Bi effectively incorporates into the $(Sb_{1-x}Bi_x)_2Se_3$ structure, while the rest still remains as the pure Bi_2Se_3 phase or as non-reacted metallic Bi. Eventually, at 340 °C (Fig. 5, t3), the formation of $(Sb_{0.8}Bi_{0.2})_2Se_3$ solid solution is denoted by a shift of the ~175 cm^{-1} band towards lower

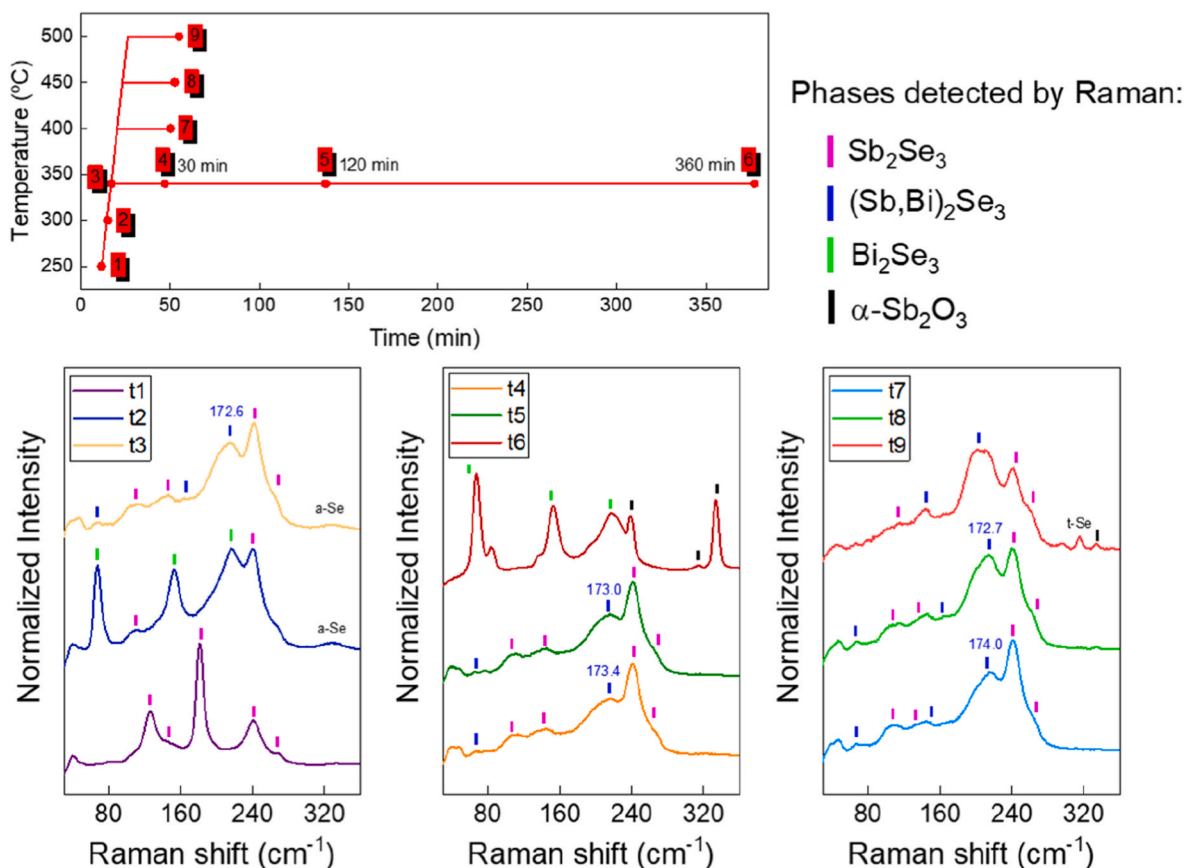**Fig. 6.** Normalized Raman spectra of the surface of $(Sb_{0.8}Bi_{0.2})_2Se_3$ thin films for different temperatures and annealing times. For these samples, the reactive annealing was interrupted after different times t1 to t9 (see Temperature vs. time plot for a description of each process).

wavenumber (172.6 cm^{-1}), together with a significant decrease of intensity of other Bi_2Se_3 peaks. With increasing the annealing dwell time (30 min and 2h – Fig. 5, t4 and t5), samples become highly uniform in terms of lateral homogeneity, and no changes in phase content can be detected. However, the amount of Bi incorporated in the solid solution at the samples' surface seems to decrease – the 172.6 cm^{-1} peak shifts back to a higher wavenumber. Additionally, the peak related to amorphous Se (a-Se), presented in the previous steps (t2 and t3), disappears with increasing of dwell time. Finally, with 6h dwell time (Fig. 5, t6), the material appears to be completely decomposed into rhombohedral
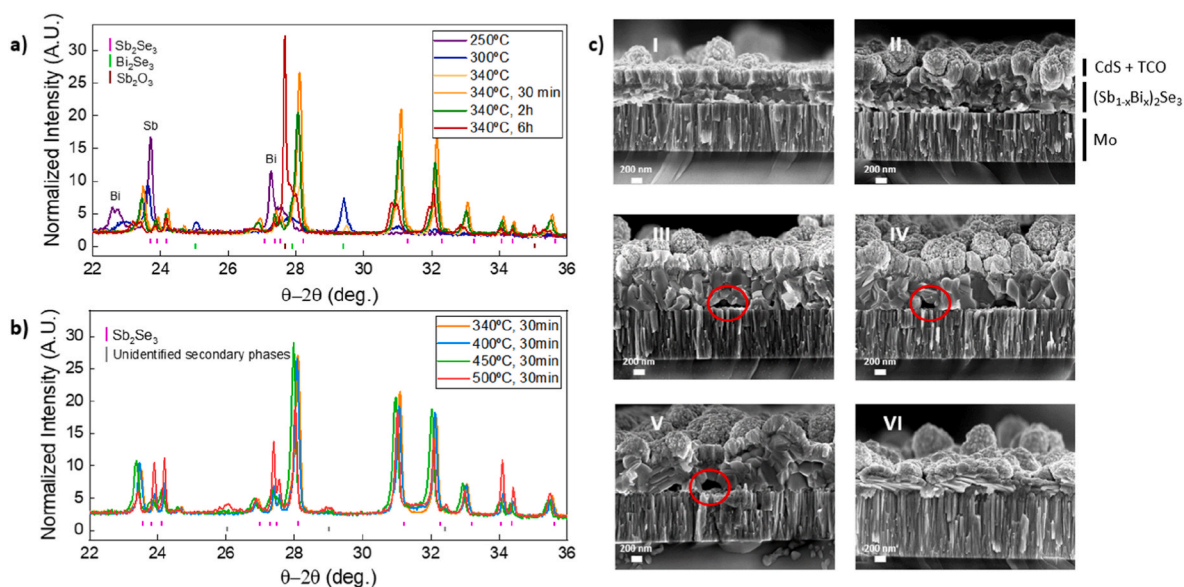

Fig. 7. X-ray diffractograms of selected Mo/$(Sb_{0.8}Bi_{0.2})_2Se_3$ thin films for different annealing conditions: **a)** Temperature from 250 °C to 340 °C with different dwell time; **b)** Temperature from 340 °C to 500 °C at t = 30min. **c)** Cross-sectional SEM micrographs of Mo/$(Sb_{0.8}Bi_{0.2})_2Se_3$/CdS/ITO devices prepared with different annealing conditions (see the main text for a detailed nomenclature description).

Bi_2Se_3 (peaks at 72, 130 and 175 cm^{-1}) and α-Sb_2O_3. Also, traces of $(Sb_{1-x}Bi_x)_2Se_3$ and/or Sb_2Se_3 phases cannot be discarded. Therefore, it seems feasible that with long annealing treatments (>2h), the solid solution decomposes into Bi_2Se_3 and Sb, which forms the oxide, and Se sublimation. On the other hand, increase of the annealing temperature to 400 and 450 °C (Fig. 5, t7 and t8) has a less pronounced effect on the Raman spectra, with only some changes in the peak assigned to the $(Sb_{1-x}Bi_x)_2Se_3$ solid solution (insignificant changes in the spectra of t4 and t7 steps, and slight redshift down to 172.7 cm^{-1} in the t8 spectrum, denoting a slight increase of Bi in the solid solution at 450 °C). Further increased temperature to 500 °C (Fig. 5, t9) results in a more pronounced redshift of the $(Sb_{1-x}Bi_x)_2Se_3$ peak (close to 168 cm^{-1}), indicating an increase of Bi content due to the appearance of α-Sb_2O_3 and trigonal Se phase (t-Se), also indicating decomposition of the solid solution, or at least a decrease of Sb and Se contents.
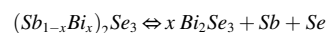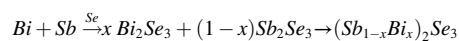
The conclusions extracted from the Raman analysis were further investigated by XRD, see Fig. 7 (complete diffractograms in Fig. S6). When the sample is subjected to 250 °C (Fig. 7a), mainly the Bragg reflections corresponding to metallic Sb (23.7° and 44.4°) and Bi (22.6° and 27.6°) are detected, plus weak reflections compatible with pure Sb_2Se_3 (e.g. 211 peak at ~28°). It is therefore confirmed that under these conditions, only partial Sb selenization occurs, while large amounts of Sb and Bi precursor remain unreacted. Increasing temperature to 300 °C leads to almost disappearance of Bi reflections, but metallic Sb is still clearly detected (note peaks at 23.7 and 44.4°). Interestingly, for this sample, the Sb_2Se_3 peaks are still weak and difficult to identify unequivocally, while the rhombohedral Bi_2Se_3 is clearly detected, showing sharp and intense reflections. At 340 °C, the Bi_2Se_3 reflections disappear almost completely, replaced by stronger ones related to the $(Sb_{0.8}Bi_{0.2})_2Se_3$ solid solution (metallic Bi and Sb not detected anymore). Overall, these results indicate that the solid solution of $(Sb_{0.8}Bi_{0.2})_2Se_3$ is formed in two phases. First, the binary compounds –orthorhombic Sb_2Se_3 and rhombohedral Bi_2Se_3 – start appearing at annealing temperatures higher than 250 °C, with the Bi_2Se_3 phase crystallizing earlier. Second, with temperature increasing, the Bi_2Se_3 and Sb_2Se_3 phases combine to form the $(Sb_{0.8}Bi_{0.2})_2Se_3$ solid solution, almost free of any secondary phase at 340 °C. The fact that Bi_2Se_3 is formed prior to Sb_2Se_3 is consistent with our hypothesis that Bi tends to diffuse towards the surface, which gives rise to the above-mentioned Bi compositional gradient. Indeed, the melting point of Bi (271.40 °C) is significantly lower than that of Sb (630.63 °C) [80]. Hence, it is likely that when the sample reaches 270 °C, Bi starts to melt, resulting in an inhomogeneous matrix of liquid Bi and solid Sb, with Bi tending to out-diffuse towards the surface, where it reacts with Se vapours. Moreover, the formation enthalpy of Bi_2Se_3 (−a146 kJ/mol) is negative and smaller than that of Sb_2Se_3 (−a128 kJ/mol), thus the Bi_2Se_3 formation is thermodynamically favoured under these manufacturing conditions [81,82]. Using SEM imaging, it has been observed that a Bi/Sb sample subjected to alloying at 300 °C gives rise to inhomogeneous surface, with the Sb layer fragmented into islands interspersed by plateaus of Bi-rich material, whose smooth appearance suggests solidification after melting, see Fig. S7. Therefore, it seems reasonable to conclude that the movement of molten Bi during the synthesis of the material plays a relevant role in its morphology and compositional distribution.

Increasing the dwell time to 2h, crystallinity improves notably, reaching optimal conditions at T = 340 °C and t = 30 min. However, with the longer 6h annealing, $(Sb_{0.8}Bi_{0.2})_2Se_3$ peaks decrease drastically, and very intense Sb_2O_3 signals appear, in line with the previous Raman results indicating that long thermal treatments lead to complete decomposition of the solid solution. On the other hand, maintaining the optimal time of 30 min, but increasing the temperature to 450 °C, the main difference is noticed in the position of reflections, which slightly tend towards lower 2θ values, related to increasing the Bi content in the solid solution, in accordance with previous results. Nonetheless, when temperature reaches 500 °C, an ostensible deterioration in the crystalline orientation is detected. Note in Table S2b that the TC$_{002}$ decreases

notably between the standard annealing treatment (340 °C, 30 min) and the 500 °C treatment (1.24 for t4, 0.89 for t9), whereas TC$_{230}$ increases considerably (0.45 for t4, and 1.03 for t9), indicating loss of the (00l)-preferred crystalline orientation. Also, the XRD diffractogram of the sample subjected to 500 °C shows additional peaks assigned to unidentified secondary phases that were not observed in any other layers, and that could be compatible with elemental Se and Sb oxides, suggesting possible decomposition of the solid solution and Se sublimation, as discussed earlier from the Raman analysis. Due to the complexity of the diffractograms, the presence of small amounts of binary phases cannot be ruled out either.

SEM imaging analysis of some of these samples also provides relevant information on the growth of the material, and the effect of time and temperature, see Fig. 7c (Fig. S9 for lower magnification micrographs). Images of complete devices – Mo/$(Sb_{1-x}Bi_x)_2Se_3$/CdS/i-ZnO/ITO – were acquired. When the sample is subjected to 250 °C (Fig. 7c I), the absorber shows unevenly shaped and disoriented grains, indicating incomplete selenization, however the precursor Bi and Sb layers are not clearly distinguished. As temperature increases, the thickness of $(Sb_{0.8}Bi_{0.2})_2Se_3$ phase also increases, along with the size of grains (300 °C in Fig. 7c II), showing columnar growth and orientation in the direction perpendicular to the substrate, similar to standard Sb_2Se_3 thin films (especially for samples annealed at 340 °C; Fig. 7c III – 0 min, and IV – 30 min) [83]. Nonetheless, increasing time and temperature, several voids have appeared at the Mo/$(Sb_{0.8}Bi_{0.2})_2Se_3$ interface (see red circled voids in Fig. 7c III to V – 340 °C, 2h), which might result in shunt problems and carrier collection deficiency, damaging the device performance [84–86]. At this point it seems natural to consider that the suggested Bi diffusion during the thermal treatment, resulting in inhomogeneous Bi distribution (see GDOES and SEM-EDX images in Figs. S4 and S5), together with the fact that Bi melts at ~300 °C, are the origin of the voids at the back region. Hence, in order to improve the properties of the material, specific synthesis strategies need to be devised to prevent the rapid diffusion of Bi towards the surface. Furthermore, note that the surface morphology is very rough (especially in the sample subjected to a 2h treatment, see Fig. 7c V), which could be the cause of increased carrier recombination [87]. Finally, with longer dwell times (6h – see Fig. 7c VI), the absorber appears completely degraded; the layer loses its integrity and grains change their appearance from columns to parallel stripes, suggesting decomposition of $(Sb_{1-x}Bi_x)_2Se_3$ into Sb_2O_3 and Bi_2Se_3, as shown in the XRD study (Fig. 7a).

From this formation mechanism study by interrupted growth, it has been possible to work out how the $(Sb_{1-x}Bi_x)_2Se_3$ system evolves as a function of annealing time and temperature. It has been shown that at 250 °C the Bi and Sb precursors remain mostly unreacted, with only small surface selenization, see Fig. 8b. Then, at 300 °C, the binary compounds Sb_2Se_3 and Bi_2Se_3 are formed first, with Bi_2Se_3 appearing at lower temperatures. This could be due to the melting of Bi at 270 °C, giving rise to a Sb–Bi solid-liquid system in which molten Bi diffuses towards the surface and becomes selenized in the first place, see Fig. 8c and d. Subsequently, when temperature reaches 340 °C, the binary compounds combine to form the $(Sb_{1-x}Bi_x)_2Se_3$ solid solution, presenting a single orthorhombic crystalline structure under Sb-rich conditions (up to x = 0.3 no phase transition has been detected), see Fig. 8e. Finally, it has been shown that the system is unstable at extended annealing times, completely decomposing into Bi_2Se_3 and Sb, which in turn reacts with oxygen from air to form Sb_2O_3, see Fig. 8f. Overall, we show that the optimal synthesis conditions for $(Sb_{1-x}Bi_x)_2Se_3$ are 340 °C during 30 min. Accordingly, we propose the following formation and decomposition mechanism of $(Sb_{1-x}Bi_x)_2Se_3$ thin films:
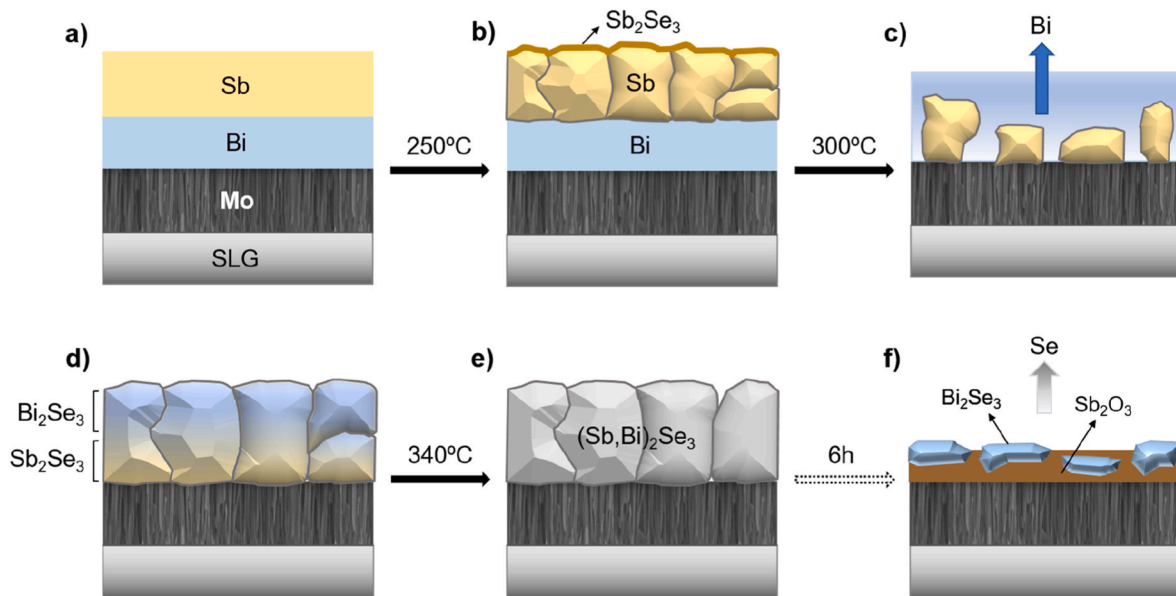
$$Bi + Sb \xrightarrow{Se} x\, Bi_2Se_3 + (1-x)Sb_2Se_3 \rightarrow (Sb_{1-x}Bi_x)_2Se_3$$

$$(Sb_{1-x}Bi_x)_2Se_3 \Leftrightarrow x\, Bi_2Se_3 + Sb + Se$$

Fig. 8. Scheme of the formation and decomposition mechanism of $(Sb_{0.8}Bi_{0.2})_2Se_3$ thin films: **a)** Bi and Sb precursors. **b)** Unreacted Bi and Sb at 250 °C. **c)** Melting and diffusion of Bi towards the surface at 300 °C. **d)** Formation of binary compounds at 300 °C (Bi-rich at the surface). **e)** Formation of $(Sb_{0.8}Bi_{0.2})_2Se_3$ solid solution at 340 °C. **f)** Decomposition into Bi_2Se_3 and Sb_2Se_3 after extended heating times (6h).

5. Improvement pathways

In this section, a new synthesis pathway has been proposed and tested in order to avoid the diffusion of Bi from the rear interface to the surface, which is likely to be the cause of its rough morphology and voids formation, see SEM images in Fig. 7c. To have more controlled layer growth, a methodology has been suggested to develop the solid solution and selenization in absence of liquid phases (melted Bi). In the first place, $(Sb_{0.8}Bi_{0.2})_2Se_3$ thin films were synthesized from Mo/Sb/Bi – inverting the order of metal evaporation, Sb was deposited first onto the Mo, and then Bi was evaporated over Mo/Sb stack. Next, the Mo/Sb/Bi precursor was subjected to the optimum annealing conditions in accordance with the previous synthesis study (340 °C during 30 min).

Accordingly, significant improvements in the optoelectronic properties have been observed, with PCE increasing to a record cell efficiency

of 1.4% (0.3% with the previous Mo/Bi/Sb stack), see Fig. 9a. Likewise, all other optoelectronic parameters undergo notable improvements; e. g., V_{oc} goes from 130 to 170 mV, roughly approaching the expected values if the V_{oc} decreases linearly when reducing the bandgap from 1.25 to 1.0 eV, see Fig. S8. Also, J_{sc} increases up to values close to those of usual Sb_2Se_3 (up to 20 mA) and FF rises by 6% points, see Fig. 9a and b. These improvements in the PV performance may arise from enhanced contact with the hole transport layer in the back of the cell and improved material quality; note that SEM images demonstrate enhanced morphology and larger grains by using the Sb/Bi precursor, see Fig. 9c. Nonetheless, XRD analysis shows that the Sb/Bi diffractogram has broader peaks and bigger shoulders than Bi/Sb's, suggesting that the new precursor gives rise to a less homogeneous composition than the former, see Fig. 9d. This result was confirmed by GDOES measurements, showing that Sb/Bi precursors lead to a more pronounced compositional
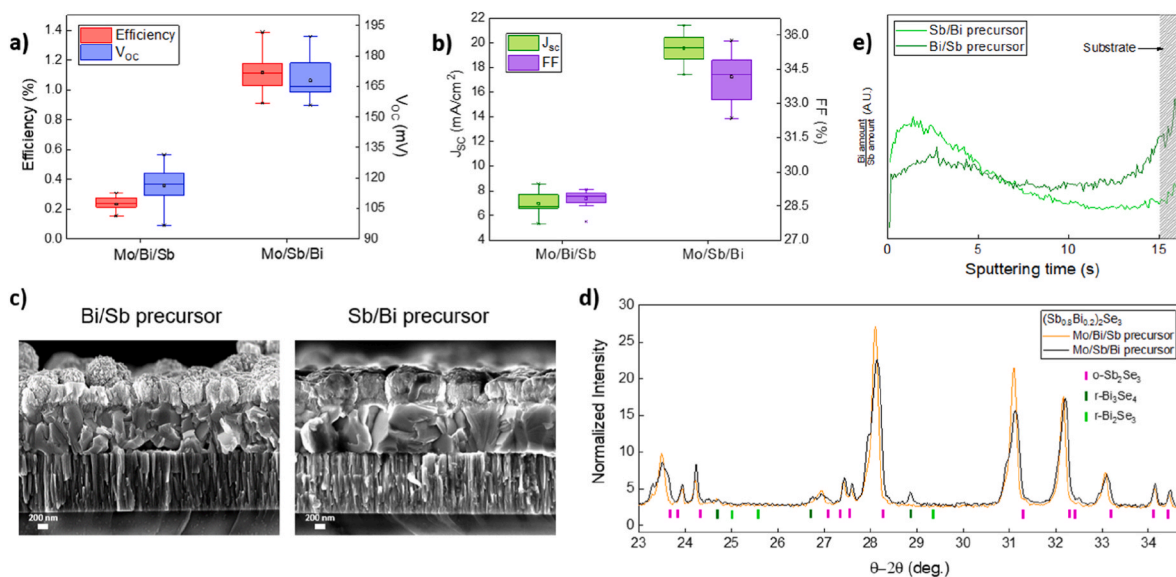

Fig. 9. Optoelectronic and structural characterization of $(Sb_{0.8}Bi_{0.2})_2Se_3$ prepared from Mo/Bi/Sb and Mo/Sb/Bi precursors. **a)** PCE and V_{oc}. **b)** J_{sc}, and FF. **c)** Cross-sectional SEM micrographs **d)** X-ray diffractograms (23°-35° range). **e)** Sb and Bi distribution in depth by GDOES measurements.

gradient than Bi/Sb – exhibiting a higher Bi content near the surface, while decreasing to nearly negligible amounts towards the back, see Fig. 9e. Also, IQE curves have a very peculiar shape and extremely low values, the integral of which does not match the J_{SC} measured with a calibrated solar simulator. This deviation may be due to the different carrier injection conditions between AM 1.5 solar simulator and IQE measurements. Indeed, by measuring the IQE under an uncalibrated whitelight bias, a significant increase in its values can be observed; and applying both white light and electric bias, high performance and standard rectangular-shaped IQE curve can be recovered, see Fig. S10. These results indicate that despite improvements in morphology and back contact, the material is likely still limited by low carrier diffusion length and high recombination, which severely limits carrier extraction in low injection conditions. The influence of light bias suggests the existence of a high defect density in the Bi-richer (narrower gap) region, leading to screening of carrier collection in low injection conditions. Further physical and electronic analysis is required to thoroughly study the correlation between defects and IQE, and seek ways to thus improve the material.

6. Conclusions

Here it is shown that the bandgap of $(Sb_{1-x}Bi_x)_2Se_3$ thin films can be effectively tuned from 1.25 to 1.0 eV by increasing Bi incorporation up to x = 0.3, demonstrating PCE between 3 and 5% for $0.01 < x \leq 0.10$. However, a significant deterioration in the optoelectronic parameters has been observed for larger Bi amounts. From dark JV curves analysis, it has been suggested that the material is essentially limited by defect-assisted bulk recombination. Furthermore, SCAPS simulations suggest that increasing the Bi amount may lead to increased bulk recombination (resulting in the reported abrupt decrease of IQE intensity) possibly due to the increasing concentration of Bi_i deep recombination centres; whereas low Bi content and Sb_2Se_3 thin films are mostly limited by interface recombination. On the other hand, Raman and XRD analyses have shown that the solid solution possesses orthorhombic structure, with small amount of pure Bi_2Se_3 phase. However, its inhomogeneous Bi distribution leads to an in-depth compositional gradient. Secondly, we have performed a formation mechanism study by interrupted growth synthesis. Accordingly, it has been possible to determine how the $(Sb_{1-x}Bi_x)_2Se_3$ solid solution evolves as a function of annealing time and temperature: i.e. the binary compounds Sb_2Se_3 and Bi_2Se_3 are formed first, with Bi_2Se_3 appearing at lower temperatures due to the lower melting temperature of Bi, which is also the cause of rapid diffusion of Bi towards the surface, resulting in the formation of voids at the rear interface, and coarse morphology. When temperature increases to 340 °C, the binary compounds combine to form the $(Sb_{1-x}Bi_x)_2Se_3$ solution, which decomposes into Bi_2Se_3 and Sb_2O_3 upon prolonged heating. Considering the conclusions of this study, it has been proven that avoiding Bi diffusion during growth allows to improve morphology and optoelectronic properties, achieving a record cell efficiency higher than 1% for x > 0.2.

Overall, this work demonstrates the potential of $(Sb_{1-x}Bi_x)_2Se_3$ as a chalcogenide-based absorber for narrow bandgap devices, with possible applications in PV and beyond (such as thermoelectrics and infrared sensing); pointing towards its current shortcomings and suggesting strategies to enhance its quality and performance. The analysis of dark JV curves by the two-diode model proved that there is a correlation between ideality factor and the disorder within the material. Finally, the synthesis study has allowed to establish a clear image of the formation mechanism, opening the door to implementing innovative routes towards developing novel quasi-1D chalcogenides with tuneable optical properties.

CRediT authorship contribution statement

Ivan Caño: Writing – original draft, Methodology, Investigation,

Formal analysis, Data curation, Conceptualization. **Pedro Vidal-Fuentes:** Methodology, Investigation, Formal analysis, Data curation. **Axel Gon Medaille:** Software. **Zacharie Jehl:** Writing – review & editing, Software, Investigation, Conceptualization. **Alex Jiménez-Arguijo:** Conceptualization. **Maxim Guc:** Methodology, Investigation, Formal analysis, Data curation. **Victor Izquierdo-Roca:** Resources, Funding acquisition, Conceptualization. **Claudia Malerba:** Methodology, Investigation, Formal analysis, Data curation. **Matteo Valentini:** Methodology, Investigation, Formal analysis, Data curation. **Maykel Jiménez-Guerra:** Methodology. **Marcel Placidi:** Writing – review & editing, Supervision, Funding acquisition. **Joaquim Puigdollers:** Resources, Funding acquisition. **Edgardo Saucedo:** Writing – review & editing, Validation, Supervision, Resources, Methodology, Funding acquisition, Conceptualization.

Declaration of competing interest

The authors declare that they have no known competing financial interests or personal relationships that could have appeared to influence the work reported in this paper.

Data availability

Data will be made available on request.

Appendix A. Supplementary data

Supplementary data to this article can be found online at https://doi.org/10.1016/j.solmat.2022.112150.

References

[1] C.J. Traverse, R. Pandey, M.C. Barr, R.R. Lunt, Emergence of highly transparent photovoltaics for distributed applications, Nat. Energy 2 (2017) 849–860, https://doi.org/10.1038/s41560-017-0016-9.

[2] W. Shockley, H.J. Queisser, Detailed balance limit of efficiency of p-n junction solar cells, J. Appl. Phys. 32 (1961) 510–519, https://doi.org/10.1063/1.1736034.

[3] Y. Zhou, L. Wang, S. Chen, S. Qin, X. Liu, J. Chen, et al., Thin-film Sb2Se3 photovoltaics with oriented one-dimensional ribbons and benign grain boundaries, Nat. Photonics 9 (2015) 409–415, https://doi.org/10.1038/nphoton.2015.78.

[4] C. Chen, D.C. Bobela, Y. Yang, S. Lu, K. Zeng, C. Ge, et al., Characterization of basic physical properties of Sb2Se3 and its relevance for photovoltaics, Front. Optoelectron. 10 (2017) 18–30, https://doi.org/10.1007/s12200-017-0702-z.

[5] Z. Li, X. Liang, G. Li, H. Liu, H. Zhang, J. Guo, et al., 9.2%-Efficient core-shell structured antimony selenide nanorod array solar cells, Nat. Commun. 10 (2019) 1–9, https://doi.org/10.1038/s41467-018-07903-6.

[6] Y.C. Choi, D.U. Lee, J.H. Noh, E.K. Kim, S Il Seok, Highly improved Sb2S3 sensitized-inorganic-organic heterojunction solar cells and quantification of traps by deep-level transient spectroscopy, Adv. Funct. Mater. 24 (2014) 3587–3592, https://doi.org/10.1002/adfm.201304238.

[7] X. Wang, R. Tang, C. Jiang, W. Lian, H. Ju, G. Jiang, et al., Manipulating the electrical properties of Sb2(S,Se)3 film for high-efficiency solar cell, Adv. Energy Mater. 10 (2020) 2–7, https://doi.org/10.1002/aenm.202002341.

[8] C.N. Savory, D.O. Scanlon, The complex defect chemistry of antimony selenide, J. Mater. Chem. A Mater. 7 (2019) 10739–10744, https://doi.org/10.1039/c9ta02022e.

[9] A. Mavlonov, T. Razykov, F. Raziq, J. Gan, J. Chantana, Y. Kawano, et al., A review of Sb2Se3 photovoltaic absorber materials and thin-film solar cells, Sol. Energy 201 (2020) 227–246, https://doi.org/10.1016/j.solener.2020.03.009.

[10] M. Huang, P. Xu, D. Han, J. Tang, S. Chen, Complicated and unconventional defect properties of the quasi-one-dimensional photovoltaic semiconductor Sb 2 Se 3, ACS Appl. Mater. Interfaces 11 (2019) 15564–15572, https://doi.org/10.1021/acsami.9b01220.

[11] B. Peng, K. Xu, H. Zhang, Z. Ning, H. Shao, G. Ni, et al., 1D SbSeI, SbSI, and SbSBr with high stability and novel properties for microelectronic, optoelectronic, and thermoelectric applications, Adv. Theory Simul. 1 (2018), https://doi.org/10.1002/adts.201700005.

[12] J.N. Tiwari, R.N. Tiwari, K.S. Kim, Zero-dimensional, one-dimensional, two-dimensional and three-dimensional nanostructured materials for advanced electrochemical energy devices, Prog. Mater. Sci. 57 (2012) 724–803, https://doi.org/10.1016/j.pmatsci.2011.08.003.

[13] S. Khelifi, G. Brammertz, L. Choubrac, M. Batuk, S. Yang, M. Meuris, et al., The path towards efficient wide band gap thin-film kesterite solar cells with transparent back contact for viable tandem application, Sol. Energy Mater. Sol. Cell. (2021) 219, https://doi.org/10.1016/j.solmat.2020.110824.

[14] R. Kondrotas, C. Chen, J. Tang, Sb2S3 solar cells, Joule 2 (2018) 857–878, https://doi.org/10.1016/j.joule.2018.04.003.

[15] J. Zhang, W. Lian, Y. Yin, X. Wang, R. Tang, C. Qian, et al., All antimony chalcogenide tandem solar cell, Solar RRL 4 (2020) 1–6, https://doi.org/10.1002/solr.202000048.

[16] T. Kirchartz, U. Rau, What makes a good solar cell? Adv. Energy Mater. 8 (2018) https://doi.org/10.1002/aenm.201703385.

[17] J. Di, J. Xia, H. Li, S. Guo, S. Dai, Bismuth oxyhalide layered materials for energy and environmental applications, Nano Energy 41 (2017) 172–192, https://doi.org/10.1016/j.nanoen.2017.09.008.

[18] H. Shi, W. Ming, M.H. Du, Bismuth chalcohalides and oxyhalides as optoelectronic materials, Phys. Rev. B 93 (2016) 1–7, https://doi.org/10.1103/PhysRevB.93.104108.

[19] R. Nishikubo, H. Kanda, I. García-Benito, A. Molina-Ontoria, G. Pozzi, A.M. Asiri, et al., Optoelectronic and energy level exploration of bismuth and antimony-based materials for lead-free solar cells, Chem. Mater. 32 (2020) 6416–6424, https://doi.org/10.1021/acs.chemmater.0c01503.

[20] S. Inagaki, M. Nakamura, H. Hatada, R. Nishino, F. Kagawa, Y. Tokura, et al., Growth of visible-light-responsive ferroelectric SbSI thin films by molecular beam epitaxy, Appl. Phys. Lett. 116 (2020), https://doi.org/10.1063/1.5142642.

[21] C. Wang, S. Xiao, X. Xiao, H. Zhu, L. Zhou, Y. Wang, et al., Nonlinear optical response of SbSI nanorods dominated with direct band gaps, J. Phys. Chem. C 125 (2021) 15441–15447, https://doi.org/10.1021/acs.jpcc.1c04282.

[22] R. Nie, H.S. Yun, M.J. Paik, A. Mehta, B.W. Park, Y.C. Choi, et al., Efficient solar cells based on light-harvesting antimony sulfoiodide, Adv. Energy Mater. 8 (2018) 1–7, https://doi.org/10.1002/aenm.201701901.

[23] J.F. Alward, C.Y. Fong, W. El-Batanouny, F. Wooten, Electronic and optical properties of SbSBr, SbSI and SbSeI, Solid State Commun. 25 (1978) 307–310, https://doi.org/10.1016/0038-1098(78)90964-X.

[24] D.v. Chepur, D.M. Bercha, I.D. Turyanitsa, V.Y. Slivka, Peculiarities of the energy spectrum and edge absorption in the chain compounds AVBVICVII, Phys. Status Solidi 30 (1968) 461–468, https://doi.org/10.1002/pssb.19680300206.

[25] S.A. Park, M.Y. Kim, J.Y. Lim, B.S. Park, J.D. Koh, W.T. Kim, Optical properties of undoped and V-doped VA-VIA-VIIA single crystals, Phys. Status Solidi 187 (1995) 253–260, https://doi.org/10.1007/BF01151535.

[26] R. Tang, X. Wang, W. Lian, J. Huang, Q. Wei, M. Huang, et al., Hydrothermal deposition of antimony selenosulfide thin films enables solar cells with 10% efficiency, Nat. Energy 5 (2020) 587–595, https://doi.org/10.1038/s41560-020-0652-3.

[27] X.Y. Ma, L. Liu, W.L. Mo, H. Liu, H.Z. Kou, Y. Wang, Surfactant-assisted solvothermal synthesis of Bi2S3 nanorods, J. Cryst. Growth 306 (2007) 159–165, https://doi.org/10.1016/j.jcrysgro.2007.03.062.

[28] C.D. Lokhande, A.U. Ubale, P.S. Patil, Thickness dependent properties of chemically deposited Bi2S3 thin films, Thin Solid Films 302 (1997) 1–4, https://doi.org/10.1016/S0040-6090(96)09540-5.

[29] R. Nie, J. Im, S Il Seok, Efficient solar cells employing light-harvesting Sb 0.67 Bi 0.33 SI, Adv. Mater. 31 (2019) 1–8, https://doi.org/10.1002/adma.201808344.

[30] S. Li, L. Xu, X. Kong, T. Kusunose, N. Tsurumachi, Q. Feng, Bismuth chalcogenide iodides Bi13S18I2 and BiSI: solvothermal synthesis, photoelectric behavior, and photovoltaic performance, J. Mater. Chem. C Mater. 8 (2020) 3821–3829, https://doi.org/10.1039/c9tc05139b.

[31] D. Tiwari, F. Cardoso-Delgado, D. Alibhai, M. Mombrú, D.J. Fermín, Photovoltaic performance of phase-pure orthorhombic BiSI thin-films, ACS Appl. Energy Mater. 2 (2019) 3878–3885, https://doi.org/10.1021/acsaem.9b00544.

[32] S.C. Hyun, Y.G. Kim, M.Y. Kim, J.D. Koh, B.S. Park, W.T. Kim, Optical properties of undoped and chromium-doped VA-VIIA single crystals, J. Mater. Sci. 30 (1995) 6113–6117, https://doi.org/10.1007/BF01151535.

[33] X. Wen, C. Chen, S. Lu, K. Li, R. Kondrotas, Y. Zhao, et al., Vapor transport deposition of antimony selenide thin film solar cells with 7.6% efficiency, Nat. Commun. 9 (2018), https://doi.org/10.1038/s41467-018-04634-6.

[34] K. Yang, B. Li, G. Zeng, Structural, morphological, compositional, optical and electrical properties of Sb2Se3 thin films deposited by pulsed laser deposition, Superlattice. Microst. 145 (2020), 106618, https://doi.org/10.1016/j.spmi.2020.106618.

[35] M. Birkett, W.M. Linhart, J. Stoner, L.J. Phillips, K. Durose, J. Alaria, et al., Band gap temperature-dependence of close-space sublimation grown Sb2Se3 by photo-reflectance, Apl. Mater. 6 (2018), https://doi.org/10.1063/1.5027157.

[36] T.P. Weiss, P. Arnou, M. Melchiorre, M. Guennou, D. Siopa, C. Pauly, et al., Thin-film (Sb,Bi)2Se3 Semiconducting layers with tunable band gaps below 1 ev for photovoltaic applications thin-film (Sb,Bi)2Se3semiconducting layers. Thomas Paul Weiss et al, Phys. Rev. Appl. 14 (2020) 1–11, https://doi.org/10.1103/PhysRevApplied.14.024014.

[37] S. Wang, Y. Sun, J. Yang, B. Duan, L. Wu, W. Zhang, et al., High thermoelectric performance in Te-free (Bi,Sb)2Se3: via structural transition induced band convergence and chemical bond softening, Energy Environ. Sci. 9 (2016) 3436–3447, https://doi.org/10.1039/c6ee02674e.

[38] J. Li, B. Wang, F. Liu, J. Liu, M. Jia, Y. Lai, et al., Structural and optical properties of electrodeposited Bi 2-xSbxSe3 thin films, ECS Solid State Lett. 1 (2012) 31–33, https://doi.org/10.1149/2.001203ssl.

[39] R.J. Cava, H. Ji, M.K. Fuccillo, Q.D. Gibson, Y.S. Hor, Crystal structure and chemistry of topological insulators, J. Mater. Chem. C Mater. 1 (2013) 3176–3189, https://doi.org/10.1039/c3tc30186a.

[40] Y. Sharma, P. Srivastava, A. Dashora, L. Vadkhiya, M.K. Bhayani, R. Jain, et al., Electronic structure, optical properties and Compton profiles of Bi 2S 3 and Bi 2Se 3, Solid State Sci. 14 (2012) 241–249, https://doi.org/10.1016/j.solidstatesciences.2011.11.025.

[41] K. Kadel, L. Kumari, W.Z. Li, J.Y. Huang, P.P. Provencio, Synthesis and thermoelectric properties of Bi2Se3 nanostructures, Nanoscale Res. Lett. 6 (2011) 1–7, https://doi.org/10.1007/s11671-010-9795-7.

[42] M. Fang, Z. Wang, H. Gu, B. Song, Z. Guo, J. Zhu, et al., Complex optical conductivity of Bi2Se3thin film: approaching two-dimensional limit, Appl. Phys. Lett. 118 (2021) 1–7, https://doi.org/10.1063/5.0049170.

[43] M.A. Tumelero, L.C. Benetti, E. Isoppo, R. Faccio, G. Zangari, A.A. Pasa, Electrodeposition and ab initio studies of metastable orthorhombic Bi2Se3: a novel semiconductor with bandgap for photovoltaic applications, J. Phys. Chem. C 120 (2016) 11797–11806, https://doi.org/10.1021/acs.jpcc.6b02559.

[44] P. Orgiani, C. Bigi, P. Kumar Das, J. Fujii, R. Ciancio, B. Gobaut, et al., Structural and electronic properties of Bi2Se3 topological insulator thin films grown by pulsed laser deposition, Appl. Phys. Lett. 110 (2017) 1–5, https://doi.org/10.1063/1.4982207.

[45] S.K. Jerng, K. Joo, Y. Kim, S.M. Yoon, J.H. Lee, M. Kim, et al., Ordered growth of topological insulator Bi2Se3 thin films on dielectric amorphous SiO2 by MBE, Nanoscale 5 (2013) 10618–10622, https://doi.org/10.1039/c3nr03032f.

[46] P.B. Souza, M.A. Tumelero, R. Faccio, R. Ahmed, C.C. Plá Cid, G. Zangari, et al., Vibrational properties of the Bi2Se3 orthorhombic metastable phase, ArXiv preprint (2020), arXiv:2008.08994.

[47] R. Ahmed, M.G. Rosul, Y. Xu, M. Zebarjadi, G. Zangari, Morphology and seebeck coefficients of electrodeposited Bi2Se3 films grown onto Au(111)/Si substrates, Electrochim. Acta 368 (2021), 137554, https://doi.org/10.1016/j.electacta.2020.137554.

[48] Y. Liu, C. Chong, W. Chen, J.A. Huang, C. Cheng, K. Tsuei, et al., Growth and characterization of MBE-grown (Bi1-xSn)2Se3 topological insulator, Jpn. J. Appl. Phys. 56 (2017) 3–7, https://doi.org/10.7567/JJAP.56.070311.

[49] J. Liu, D. Vanderbilt, Topological phase transitions in (Bi1-xInx) 2Se3 and (Bi1-xSbx) 2Se3, Phys. Rev. B Condens. Matter 88 (2013) 1–12, https://doi.org/10.1103/PhysRevB.88.224202.

[50] R. Huang, J. Zhang, F. Wei, L. Shi, T. Kong, G. Cheng, Ultrahigh responsivity of ternary Sb-Bi-Se nanowire photodetectors, Adv. Funct. Mater. 24 (2014) 3581–3586, https://doi.org/10.1002/adfm.201304176.

[51] C.H. Lee, R. He, Z. Wang, R.L.J. Qiu, A. Kumar, C. Delaney, et al., Metal-insulator transition in variably doped (Bi1-xSb x)2Se3 nanosheets, Nanoscale 5 (2013) 4337–4343, https://doi.org/10.1039/c3nr01155k.

[52] P. Vidal-Fuentes, M. Placidi, Y. Sánchez, I. Becerril-Romero, J. Andrade-Arvizu, Z. Jehl, et al., Efficient Se-rich Sb2Se3/CdS planar heterojunction solar cells by sequential processing: control and influence of Se content, Solar RRL 4 (2020) 1–11, https://doi.org/10.1002/solr.202000141.

[53] I. Caño, P. Vidal-Fuentes, L. Calvo-Barrio, X. Alcobé, J.M. Asensi, S. Giraldo, et al., Does Sb2Se3 admit nonstoichiometric conditions? How modifying the overall Se content affects the structural, optical, and optoelectronic properties of Sb2Se3 thin films, ACS Appl. Mater. Interfaces 14 (2022) 11222–11234, https://doi.org/10.1021/acsami.1c20764.

[54] M. Fang, Z. Wang, H. Gu, M. Tong, B. Song, X. Xie, et al., Layer-dependent dielectric permittivity of topological insulator Bi2Se3 thin films, Appl. Surf. Sci. 509 (2020), https://doi.org/10.1016/j.apsusc.2019.144822.

[55] Y. Chen, Y. Wang, R. Wang, X. Hu, J. Tao, G.E. Weng, et al., Importance of interfacial passivation in the high efficiency of Sb2Se3 thin-film solar cells: numerical evidence, ACS Appl. Energy Mater. 3 (2020) 10415–10422, https://doi.org/10.1021/acsaem.0c01203.

[56] R.M. Geisthardt, M. Topič, J.R. Sites, Status and potential of CdTe solar-cell efficiency, IEEE J. Photovoltaics 5 (2015) 1217–1221, https://doi.org/10.1109/JPHOTOV.2015.2434594.

[57] T. Ghorbani, M. Zahedifar, M. Moradi, E. Ghanbari, Influence of affinity, band gap and ambient temperature on the efficiency of CIGS solar cells, Optik 223 (2020), 165541, https://doi.org/10.1016/j.ijleo.2020.165541.

[58] Y. Sun, K.H. Montgomery, X. Wang, S. Tomasulo, M.L. Lee, P. Bermel, in: Modeling Wide Bandgap GaInP Photovoltaic Cells for Conversion Efficiencies up to 16.5%.

2015 IEEE 42nd Photovoltaic Specialist Conference, PVSC, 2015 2015, https://doi.org/10.1109/PVSC.2015.7356074.

[59] P. Würfel, U. Würfel, Physics of Solar Cells. From Basic Principles to Advanced Concepts, Wiley-VCH, 2016.

[60] D. Abou-Ras, T. Kirchartz, U. Rau, Advanced Characterization Techniques for Thin Film Solar Cells, second ed. vol. 1–2, 2016, https://doi.org/10.1002/9783527699025.

[61] M.L. Megherbi, F. Pezzimenti, L. Dehimi, A. Saadoune, F.G. Della Corte, Analysis of the forward I–V characteristics of Al-implanted 4H-SiC p-i-n diodes with modeling of recombination and trapping effects due to intrinsic and doping-induced defect states, J. Electron. Mater. 47 (2018) 1414–1420, https://doi.org/10.1007/s11664-017-5916-8.

[62] K.R. McIntosh, P.P. Altermatt, G. Heiser, Depletion-region recombination in silicon solar cells: when does mdr = 2? 16th European photovoltaic, Solar Energy Conference (2000) 250–253, 0.

[63] A. Cuevas, The recombination parameter J0, Energy Proc. 55 (2014) 53–62, https://doi.org/10.1016/j.egypro.2014.08.073.

[64] O. Breitenstein, P. Altermatt, K. Ramspeck, a Schenk, The origin of ideality factors n>2 of shunts and surfaces in the dark I-V curves of solar cells, in: 21st European Photovoltaic Solar Energy Conference, 625–8, 2006.

[65] O. Breitenstein, P. Altermatt, K. Ramspeck, M.A. Green, J. Zhao, A. Schenk, Interpretation of the commonly observed I-V characteristics of C-SI cells having ideality factor larger than two. Conference Record of the 2006 IEEE 4th World Conference on Photovoltaic Energy Conversion, WCPEC-4 1 (2006) 879–884, https://doi.org/10.1109/WCPEC.2006.279597.

[66] M. Nardone, V.G. Karpov, D. Shvydka, M.L.C. Attygalle, Theory of electronic transport in noncrystalline junctions, J. Appl. Phys. 106 (2009), https://doi.org/10.1063/1.3213336.

[67] Y. Chen, Y. Wang, R. Wang, X. Hu, J. Tao, G.E. Weng, et al., Importance of interfacial passivation in the high efficiency of Sb2Se3 thin-film solar cells: numerical evidence, ACS Appl. Energy Mater. 3 (2020) 10415–10422, https://doi.org/10.1021/acsaem.0c01203.

[68] A. Gon Medaille, K.J. Tiwari, S. Giraldo, M. Placidi, E. Saucedo, Z. Jehl Li-Kao, Numerical investigation of interface passivation strategies for Sb 2 Se 3/CdS solar cells, Solar RRL (2021), 2100911, https://doi.org/10.1002/solr.202100911.

[69] S.S. Hegedus, W.N. Shafarman, Thin-film solar cells: device measurements and analysis, Prog. Photovoltaics Res. Appl. 12 (2004) 155–176, https://doi.org/10.1002/pip.518.

[70] N. Fleck, T.D.C. Hobson, C.N. Savory, J. Buckeridge, T.D. Veal, M.R. Correia, et al., Identifying Raman modes of Sb2Se3 and their symmetries using angle-resolved polarised Raman spectra, J. Mater. Chem. A Mater. 8 (2020) 8337–8344, https://doi.org/10.1039/d0ta01783c.

[71] P. Vidal-Fuentes, M. Guc, X. Alcobe, T. Jawhari, M. Placidi, A. Pérez-Rodríguez, et al., Multiwavelength excitation Raman scattering study of Sb2Se3 compound: fundamental vibrational properties and secondary phases detection, 2D Mater. 6 (2019), https://doi.org/10.1088/2053-1583/ab4029.

[72] A. Shongalova, M.R. Correia, B. Vermang, J.M.V. Cunha, P.M.P. Salomé, P. A. Fernandes, On the identification of Sb2Se3 using Raman scattering, MRS Commun 8 (2018) 865–870, https://doi.org/10.1557/mrc.2018.94.

[73] B. Irfan, S. Sahoo, A.P.S. Gaur, M. Ahmadi, M.J.F. Guinel, R.S. Katiyar, et al., Temperature dependent Raman scattering studies of three dimensional topological insulators Bi2Se3, J. Appl. Phys. 115 (2014), https://doi.org/10.1063/1.4871860.

[74] I.F. Chang, A.S.S. Mrtaa, Application of a modified random-element-isodisplacement model to long-wavelength optic phonons of mixed crystals, Phys. Rev. 172 (1968) 924–933.

[75] D. Lee, J.Y. Cho, J. Heo, Improved efficiency of Sb2Se3/CdS thin-film solar cells: the effect of low-temperature pre-annealing of the absorbers, Sol. Energy 173 (2018) 1073–1079, https://doi.org/10.1016/j.solener.2018.08.065.

[76] Z. Li, X. Chen, H. Zhu, J. Chen, Y. Guo, C. Zhang, et al., Sb2Se3 thin film solar cells in substrate configuration and the back contact selenization, Sol. Energy Mater. Sol. Cell. 161 (2017) 190–196, https://doi.org/10.1016/j.solmat.2016.11.033.

[77] Z. Cai, S. Chen, Extrinsic dopants in quasi-one-dimensional photovoltaic semiconductor Sb2S3: a first-principles study, J. Appl. Phys. 127 (2020), https://doi.org/10.1063/1.5140751.

[78] N. Fleck, T.D.C. Hobson, C.N. Savory, J. Buckeridge, T.D. Veal, M.R. Correia, et al., Identifying Raman modes of Sb2Se3 and their symmetries using angle-resolved polarised Raman spectra, J. Mater. Chem. A Mater. 8 (2020) 8337–8344, https://doi.org/10.1039/d0ta01783c.

[79] F. Pattini, S. Rampino, F. Mezzadri, D. Calestani, G. Spaggiari, M. Sidoli, et al., Role of the substrates in the ribbon orientation of Sb2Se3 films grown by Low-Temperature Pulsed Electron Deposition, Sol. Energy Mater. Sol. Cell. 218 (2020), 110724, https://doi.org/10.1016/j.solmat.2020.110724.

[80] S. Budavari, The Merck Index : an Encyclopedia of Chemicals, Drugs, and Biologicals, twelfth ed., Merck Research Laboratories, New Jersey, 1996.

[81] A. Olin, B. Noläng, E.G. Osadchi, L.-O. Öhman, E. Rosén, Chemical Thermodynamics of Selenium, 2005.

[82] D.R. Lide, CRC Handbook of Chemistry and Physics, 84th edition, 2004, https://doi.org/10.1136/oem.53.7.504.

[83] R. Krautmann, N. Spalatu, R. Gunder, D. Abou-Ras, T. Unold, S. Schorr, et al., Analysis of grain orientation and defects in Sb2Se3 solar cells fabricated by close-spaced sublimation, Sol. Energy 225 (2021) 494–500, https://doi.org/10.1016/j.solener.2021.07.022.

[84] F. Liu, J. Huang, K. Sun, C. Yan, Y. Shen, J. Park, et al., Beyond 8% ultrathin kesterite Cu2ZnSnS4 solar cells by interface reaction route controlling and self-organized nanopattern at the back contact, NPG Asia Mater. 9 (2017), https://doi.org/10.1038/am.2017.103.

[85] S. Giraldo, E. Saucedo, M. Neuschitzer, F. Oliva, M. Placidi, X. Alcobé, et al., How small amounts of Ge modify the formation pathways and crystallization of kesterites, Energy Environ. Sci. 11 (2018) 582–593, https://doi.org/10.1039/c7ee02318a.

[86] S. Giraldo, R. Fonoll-Rubio, Z. Jehl Li-Kao, Y. Sánchez, L. Calvo-Barrio, V. Izquierdo-Roca, et al., Rear interface engineering of kesterite Cu2ZnSnSe4 solar cells by adding CuGaSe2 thin layers, Prog. Photovoltaics Res. Appl. 29 (2021) 334–343, https://doi.org/10.1002/pip.3366.

[87] K.B. Cheon, S.K. Hwang, S.W. Seo, J.H. Park, M.A. Park, J.Y. Kim, Roughness-controlled Cu2ZnSn(S,Se)4 thin-film solar cells with reduced charge recombination, ACS Appl. Mater. Interfaces 11 (2019) 24088–24095, https://doi.org/10.1021/acsami.9b05852.